

Monazite Dating of Prograde and Retrograde P – T – d paths in the Barrovian terrane of the Thaya window, Bohemian Massif

P. Štípská^{1,2*}, B. R. Hacker³, M. Racek^{4,5}, R. Holder³,
A. R. C. Kylander-Clark³, K. Schulmann^{1,2} and P. Hasalová²

¹Ecole et Observatoire des Sciences de la Terre, Institut de Physique du Globe de Strasbourg–CNRS UMR7516, Université de Strasbourg, 1 rue Blessig, F-67084, Strasbourg Cedex, France, ²Center for Lithospheric Research, Czech Geological Survey, 11821 Praha 1, Czech Republic, ³Department of Earth Science, University of California, Santa Barbara, CA 93106, USA, ⁴Regional Geology of Crystalline Complexes Department, Czech Geological Survey, 11821 Praha 1, Czech Republic and ⁵Institute of Petrology and Structural Geology, Charles University in Prague, Albertov 6, Praha 2, 12800, Czech Republic

*Corresponding author. Telephone: +420257089492. Fax: +420 257 089 500.
E-mail: pavla.stipska@geology.cz

Received October 20, 2014; Accepted May 7, 2015

ABSTRACT

Monazite laser ablation–split-stream inductively coupled plasma–mass spectrometry (LASS) was used to date monazite *in situ* in Barrovian-type micaschists of the Moravian zone in the Thaya window, Bohemian Massif. Petrography and garnet zoning combined with pseudosection modelling show that rocks from staurolite–chlorite, staurolite, kyanite and kyanite–sillimanite zones record burial in the S_1 fabric under a moderate geothermal gradient from 4–4.5 kbar and ~ 530 – 540°C to 5 kbar and 570°C , 6–7 kbar and 600 – 640°C , 7.5–8 kbar and 630 – 650°C , and 8 kbar and 650°C , respectively. In the kyanite and kyanite–sillimanite zones, garnet rim chemistry and local syntectonic replacement of garnet by sillimanite–biotite aggregates point to re-equilibration at 5.5–6 kbar and 630 – 650°C in the S_2 fabric. Heterogeneously developed retrograde shear zones (S_3) are marked by widespread chloritization, but minor chlorite is present in the studied samples. Monazite abundance and size increase with metamorphic grade from $5\ \mu\text{m}$ in the staurolite–chlorite zone to $>100\ \mu\text{m}$ in the kyanite and kyanite–sillimanite zones. Irrespective of the monazite-forming reaction, this is interpreted as the onset of limited prograde monazite growth at staurolite grade, and continued prograde monazite growth after the kyanite-in reaction, compatible with conditions of about 5.5 kbar and 570°C and 7.5 kbar and 630°C from pseudosection modelling. Monazite is zoned, showing embayments and sharp boundaries between zones, with low Y in the staurolite zone, high-Y cores and low-Y rims in the kyanite zone, and high-Y cores, a low-Y mantle and a high-Y rim in the sillimanite zone. The ^{207}Pb -corrected $^{238}\text{U}/^{206}\text{Pb}$ ages from three samples range from 344 ± 7 to 330 ± 7 Ma, irrespective of metamorphic grade. The dates from monazite inclusions are interpreted as the ages of the staurolite- and kyanite-in reactions along the prograde path at 340 and 337 ± 7 Ma, respectively. The monazite in the matrix (and some inclusions) is interpreted as dating the prograde crystallization at $(340$ – $337) \pm 7$ Ma within the S_1 fabric, and then being affected by recrystallization at or down to 332 ± 7 Ma in the S_2 and S_3 fabrics. The two groups of data, for 340 – 337 and 332 Ma, are significantly different when only their in-run uncertainties (± 1 – 3 Myr) are compared and indicate a 9 ± 3 Myr period of monazite (re)crystallization. A systematic increase in heavy rare earth element (HREE) content with decreasing monazite age from 344 to 335 Ma is correlated with growth on the prograde P – T path; the drop in HREE of monazite at 335 – 328 Ma is assigned to recrystallization. The presence of chlorite even in the least retrogressed samples witnesses limited external fluid availability on the retrograde P – T path. Migration of this

fluid was probably responsible for heterogeneous fluid-assisted recrystallization and resetting of original prograde monazite, even where included in garnet, staurolite or kyanite. It is suggested that the rocks passed the chlorite-in reaction on the retrograde path at 332 ± 7 Ma. The timing of burial in the Thaya window, a deformed part of the underthrust Brunia microcontinent, was coeval with exhumation of granulites and migmatites of the Moldanubian orogenic root at c. 340 Ma.

Key words: monazite dating and REE; monazite growth and recrystallization; prograde and retrograde P - T - d - t path; Bohemian Massif; Barrovian metamorphism

INTRODUCTION

Monazite is extensively used to date metamorphism in medium-grade felsic rocks. To link monazite age to a tectonic event, attempts are made to correlate its growth with a deformational phase (Williams & Jercinovic, 2002; Dumond *et al.*, 2008; Wawrzenitz *et al.*, 2012) or more commonly with a P - T path or a P - T - d path (Vance *et al.*, 2003; Dahl *et al.*, 2005; St-Onge *et al.*, 2007; Kellett *et al.*, 2010; Weller *et al.*, 2013). For subsolidus metapelites, relations among allanite, xenotime and monazite have been used to infer P - T conditions of monazite formation, and several monazite-forming reactions have been proposed (Pyle *et al.*, 2001; Spear & Pyle, 2002; Pyle & Spear, 2003; Wing *et al.*, 2003; Janots *et al.*, 2008, 2009; Spear, 2010; Gasser *et al.*, 2012; Palin *et al.*, 2014). Another approach to inferring the P - T conditions of monazite growth is an empirical correlation of monazite presence or absence, abundance and shape with metamorphic grade. It has repeatedly been shown that detrital monazite may be present in metapelites, but usually reacts out before the garnet isograd. The first metamorphic monazite—rare, small and irregular in shape—commonly appears at the garnet isograd; at the staurolite isograd it is slightly more abundant, but small, and at the Al_2SiO_5 isograd it is abundant, large and may be euhedral (Kingsbury *et al.*, 1993; Rubatto *et al.*, 2001; Wing *et al.*, 2003; Gasser *et al.*, 2012). Monazite included in porphyroblasts such as garnet, staurolite and Al_2SiO_5 polymorphs has been interpreted as dating points on the prograde P - T path or the peak of metamorphism (Harrison *et al.*, 1997; Foster *et al.*, 2000; Catlos *et al.*, 2002, 2004; Wing *et al.*, 2003; Kohn *et al.*, 2005; Rasmussen *et al.*, 2006; Caddick *et al.*, 2007; Martin *et al.*, 2007; Hoisch *et al.*, 2008; Kellett *et al.*, 2010). Monazite progressively dissolves with increasing melting and major regrowth is presumed to occur during retrograde cooling (Kohn *et al.*, 2005; Kelsey *et al.*, 2008; Gasser *et al.*, 2012). Another complementary approach commonly used in linking monazite growth to a P - T path is correlating trace-element signatures and zoning with modal variation and/or trace-element signatures in major phases (Catlos *et al.*, 2002; Hermann & Rubatto, 2003; Kohn *et al.*, 2005; Rubatto *et al.*, 2006, 2013; Carosi *et al.*, 2010; Gasser *et al.*, 2012).

Owing to the high closure temperature for Pb diffusion in monazite (Seydoux-Guillaume *et al.*, 2002; Cherniak *et al.*, 2004), it has been generally concluded that U/Th-Pb ages record monazite growth, and thus

the ages in subsolidus metapelites have most commonly been interpreted to date points on the prograde P - T path, or points close to or at peak metamorphic conditions. Only in some cases has retrograde monazite crystallization been suggested at subsolidus conditions (e.g. Lanzirrotti & Hanson, 1996). However, especially in the past decade, it has been shown with natural examples (Ayers *et al.*, 1999; Crowley & Ghent, 1999; Poitrasson *et al.*, 2000; Townsend *et al.*, 2001; Martin *et al.*, 2007; Gasser *et al.*, 2012; Kelly *et al.*, 2012; Seydoux-Guillaume *et al.*, 2012; Didier *et al.*, 2013) and in experiments (Seydoux-Guillaume *et al.*, 2002; Harlov & Hetherington, 2010; Hetherington *et al.*, 2010; Harlov *et al.*, 2011; Williams *et al.*, 2011; Janots & Wirth, 2012) that monazite may recrystallize and change composition after growth, and that the isotopic ratios may be partially or completely reset at temperature far below 800°C. In the absence of detectable diffusion profiles this is most commonly interpreted as a result of dissolution-precipitation in the presence of fluids (Putnis, 2002; Harlov *et al.*, 2011). Thus, some monazite ages in subsolidus rocks may date prograde or peak metamorphism, but others may date the retrograde P - T path, or be meaningless. Caution is therefore needed in the interpretation of ages, with monazite trace-element chemistry, zoning, texture, reaction history, rock fabric, and petrological and geological context being considered along with the isotopic ratios (Catlos *et al.*, 2002; Vance *et al.*, 2003; Kohn *et al.*, 2005; Martin *et al.*, 2007; Kellett *et al.*, 2010; Gasser *et al.*, 2012).

Continental collisional thrust zones commonly show an inverted Barrovian metamorphic gradient with decreasing pressure and temperature conditions to the structural footwall; examples include the Himalaya (Bordet, 1961; Gansser, 1964), the Caledonian belt (Andreasson & Lagerblad, 1980), the Canadian Cordillera (Gibson *et al.*, 1999), the Appalachian belt (Camiré, 1995), the Californian range (Graham & England, 1976) and the European Variscan belt (Suess, 1912; Burg *et al.*, 1984; Arenas *et al.*, 1995; Pitra *et al.*, 2010). Combined studies of structural development, P - T evolution and geochronology allow interpretations to be made of the processes of continental deformation in space and time in these regions (e.g. Mottram *et al.*, 2014).

In this study we chose a classic domain of inverted Barrovian metamorphism at the eastern margin of the Bohemian Massif where nappe stacking was proposed

as early as 1912 by Suess. We combine the P – T – d paths of micaschists and LASS (laser ablation–split-stream inductively coupled plasma–mass spectrometry) monazite dates to discuss timescales of burial, tectonic inversion and exhumation for one of the fundamental mechanisms of continental deformation at the boundary of a hot orogenic root and a rigid microcontinent. Petrography, garnet zoning and mineral-equilibria modelling in the framework of their structural development are used to infer the prograde and retrograde P – T – d paths. Monazite abundance, size, chemistry, zoning, textural position and petrological context are described prior to LASS simultaneous measurement of isotopic ratios and rare earth elements (REE). Based on this combined approach we distinguish two populations of ages, the first dating the prograde P – T – d path close to peak metamorphic conditions in single metamorphic zones, and the second dating retrograde fluid-assisted recrystallization of prograde monazite. The relationships of the ages of tectonic processes leading to the formation of inverted Barrovian metamorphism in the Brunia microcontinent are discussed with respect to the coeval exhumation of high-grade rocks in the hanging-wall Moldanubian orogenic root.

GEOLOGICAL SETTING

The Saxothuringian oceanic and continental domain, the Teplá–Barrandian, the Moldanubian and the Brunia continental domains are the major tectonic units of the Variscan Bohemian Massif, assembled in Devonian and Carboniferous times [Fig. 1; revised from Schulmann *et al.* (2008)]. The Saxothuringian was partly subducted to the SE below the Moldanubian–Lugian domain that formed the thickened root above the subduction zone, with the Teplá–Barrandian representing its uppermost part (Schulmann *et al.*, 2009). The Moldanubian and Lugian domains are composed of north–south-trending belts of orogenic lower crust dominated by (ultra-)high-pressure granulites and migmatites (the Gföhl unit) alternating with middle to upper crustal sequences dominated by the volcano-sedimentary Varied and Monotonous groups. The alternation of the belts is explained by vertical extrusion of the granulites owing to combined lateral compression and buoyancy (Štípská *et al.*, 2004; Lexa *et al.*, 2011), and was followed by heterogeneous reworking by subhorizontal migmatitic channel flow in the middle orogenic crust (Štípská *et al.*, 2008; Schulmann *et al.*, 2009). The most common zircon date from the granulites, *c.* 340 Ma, is commonly interpreted as the peak of HP metamorphism (Kröner *et al.*, 2000; Janoušek & Holub, 2007); however, some studies suggest that this age is instead the end of HP metamorphism and the beginning of exhumation (Lexa *et al.*, 2011), and that granulites were at mid-crustal depth by *c.* 337 Ma (Friedl *et al.*, 2011). Some garnet and zircon dates have been used to propose that burial to (U)HP conditions of the granulites is older (360–350 Ma; Prince *et al.*, 2000; Tajčmanová *et al.*, 2010; Nahodilová

et al., 2014), but in the light of zircon recrystallization processes at high temperature this is controversial (Bröcker *et al.*, 2010).

The studied region is located at the eastern margin of the Bohemian Massif, forming the easternmost extremity of the Variscan belt [Fig. 1; revised from Schulmann *et al.* (2008)]. Here, underthrusting of the Brunia microcontinent (Dudek, 1980) beneath high-grade rocks of the Moldanubian–Lugian domain resulted in a 300 km long deformation front called the Moravo-Silesian zone (Suess, 1912). This zone of deformation is characterized by Barrovian inverted metamorphism and nappe stacking (e.g. Štípská & Schulmann, 1995; Fritz *et al.*, 1996; and references therein). Structurally above the Moravo-Silesian zone are the high-grade rocks of the Moldanubian domain: high-pressure granulites and migmatites that underwent vertical extrusion and are in this region strongly reworked by shallow-dipping migmatite flow (e.g. Racek *et al.*, 2006; Hasalová *et al.*, 2008; Štípská *et al.*, 2008). The Moravo-Silesian zone is separated from the Moldanubian domain by a belt of kyanite-bearing micaschists (the Micaschists zone; Suess, 1912). The Moravo-Silesian zone emerges from beneath the Moldanubian domain in three tectonic windows (from north to south): the Silesian zone, and the Svratka and the Thaya windows (Suess, 1912, 1926); the latter two are known as the Moravian zone (Figs 1 and 2).

The Svratka and Thaya windows consist of a parautochthonous basement and a *c.* 7 km thick pile of two nappes (the Lower and Upper Moravian nappes; Štípská & Schulmann, 1995) each composed of Late Proterozoic orthogneiss sheets (Friedl *et al.*, 2004) overlain by metasediments (Fig. 2). The parautochthonous and autochthonous basement is composed of the deformed Thaya and Svratka granites, Upper Proterozoic metasediments and Devonian cover. The structurally deeper nappe (the Lower Moravian nappe) is composed of the Weitersfeld orthogneiss, metapelites and marbles. The structurally higher nappe (the Upper Moravian nappe) consists of the Bíteš orthogneiss at the bottom and micaschists, quartzites, marbles and amphibolites at the top. The Micaschist zone at the top of the nappe sequence is considered to be either the uppermost part of the Upper Moravian nappe (Konopásek *et al.*, 2002) or a retrogressed part of the Moldanubian domain (Suess, 1926).

In the Moravo-Silesian zone, three main stages of tectonic evolution are described (Schulmann *et al.*, 1991; Fritz *et al.*, 1996; Ulrich *et al.*, 2002). The main metamorphic foliation S_{1-2} follows the domal shape of the tectonic windows as exemplified by the structural map of the Thaya window (Fig. 2a). The main metamorphic fabric is refolded by recumbent F_2 folds that are parallel to the main lineation (Fig. 2c; Schulmann, 1990) and reactivated by D_2 ductile shear zones mostly located at the base of the nappes, resulting in a composite foliation S_{1-2} . The first deformation (D_1) resulted from Brunia underthrusting whereas the second event

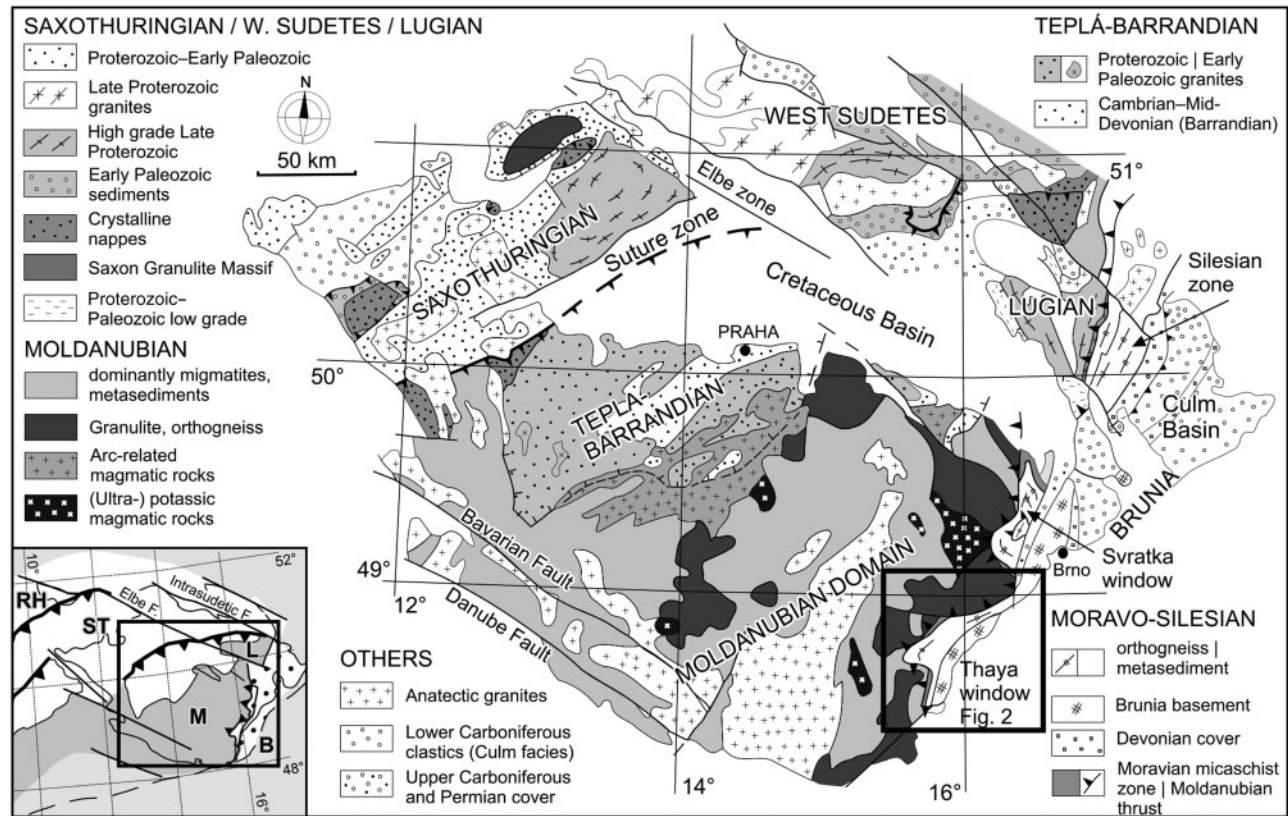


Fig. 1. Geological map of the Bohemian Massif. The location of the study area (Fig. 2) is indicated. Lower left inset shows the position of the study area in the framework of the European Variscides (modified after Edel *et al.*, 2003). RH, Rhenohercynian; ST, Saxothuringian; M, Moldanubian; B, Brunian; L, Lugian.

(D_2) is related to the emplacement of crustal nappes (Schulmann *et al.*, 1994). This was followed by crustal-scale folding (D_3) of the previously stacked nappes, forming the domal shape of the Thaya window, under greenschist-facies conditions (Štípská *et al.*, 2000).

The metamorphism increases structurally upwards from biotite to kyanite and then kyanite–sillimanite zone (Fig. 2b) (Höck, 1975; Štípská & Schulmann, 1995; Štípská *et al.*, 2000). The growth of index minerals was syntectonic with the D_1 deformation and is interpreted as a result of increasing temperature and pressure during burial of the continental margin under the Moldanubian domain (Štípská & Schulmann, 1995). Overprinting sillimanite-bearing shear zones D_2 in the kyanite zone, and localized greenschist-facies shear zones D_3 in all units show that the metamorphic inversion is related to nappe stacking and heterogeneous shearing during exhumation (Štípská & Schulmann, 1995; Fritz *et al.*, 1996). All of the structures and metamorphic zones were folded during the late D_3 event, which resulted in discordant relationships between the metamorphic isograds and the lithotectonic units (Fig. 2b) (Štípská *et al.*, 2000). Peak metamorphic conditions of 520–600°C at 5–7 kbar (staurolite zone in the Parautochthon and the Lower Moravian nappe) and 620–650°C at 6–10 kbar (kyanite zone in the Upper Moravian nappe and Micaschist zone) were inferred

from petrogenetic grids and thermobarometry (Höck *et al.*, 1990; Štípská & Schulmann, 1995), but prograde P – T paths remain unknown. Fluid inclusions in late quartz yield 300°C at 3.3–4 kbar (Fritz & Loitzenbauer, 1994). Post-nappe emplacement cooling is constrained to 325–335 Ma by $^{40}\text{Ar}/^{39}\text{Ar}$ muscovite ages (Dallmeyer *et al.*, 1992; Fritz *et al.*, 1996), but no prograde or peak metamorphic ages have been reported.

PETROGRAPHY AND MINERAL CHEMISTRY

Analytical procedure and abbreviations

Mineral analyses and compositional maps of garnet were made on a scanning electron microscope Tescan VEGA equipped with an X-Max 50 energy-dispersive spectrometry (EDS) detector (Oxford Instruments) at the Institute of Petrology and Structural Geology (Charles University in Prague) in point beam mode at 15 kV and 1.5 nA.

The sample petrography is documented in Fig. 3 and garnet zoning is shown in Fig. 4; representative mineral analyses are given in Table 1. Trends in mineral composition or zoning quoted in the text are marked with '→', and '←' designates a range of mineral compositions. Mineral abbreviations are as follows: g, garnet; sill, sillimanite; and, andalusite; ky, kyanite; cd, cordierite; bi, biotite; mu, muscovite; pa, paragonite; chl, chlorite; pl,

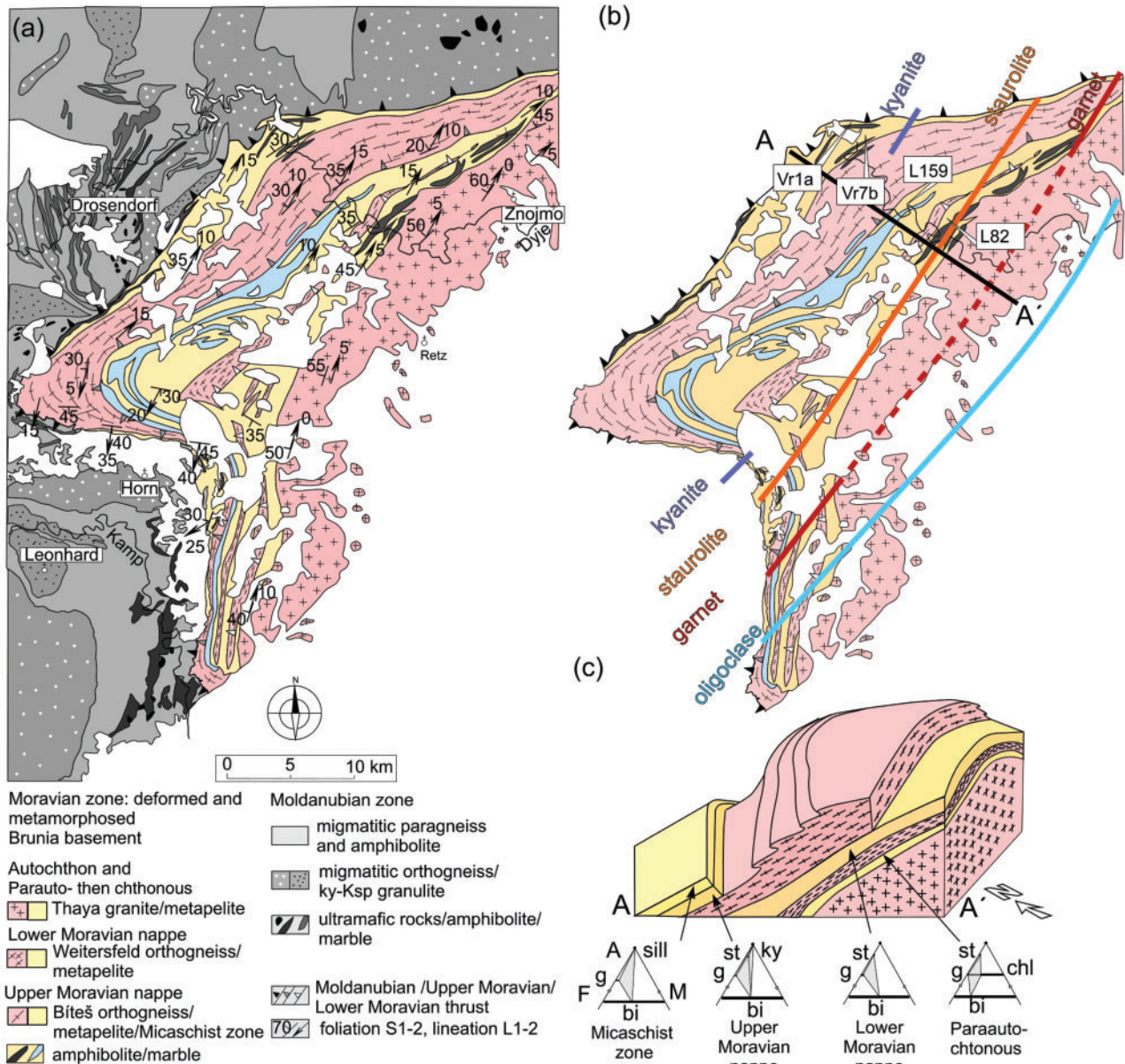


Fig. 2. Map and block-diagram of the Thaya window compiled after Höck (1975), Fuchs (1976), Štípská & Schulmann (1995) and Štípská *et al.* (2000). (a) Geological map of the area studied, showing foliation and lineation measurements. (b) Metamorphic isograds for garnet, staurolite and kyanite in metapelites and oligoclase in orthogneiss. Sample locations from this study and the position of the block diagram are indicated. (c) Interpretative block diagram with mineral assemblages indicated. Vertical axis not to scale.

plagioclase; ksp, K-feldspar; q, quartz; ilm, ilmenite; mt, magnetite; ttn, titanite; ab, albite; ep, epidote; liq, liquid; mnz, monazite.

To constrain the timing of burial metamorphism and the P – T – t – d paths, we revisited four representative samples from the various units of the Thaya window previously studied by Štípská & Schulmann (1995) (Fig. 2b). The samples were used for pseudosection modelling and U–Pb monazite geochronology. The first sample is from the Parautochthon (staurolite–chlorite zone, sample L82), the second from the Lower Moravian nappe (staurolite zone, sample L159), the third from the Upper Moravian nappe (kyanite zone, sample Vr7b), and the

fourth from the Micaschist zone (kyanite–sillimanite zone, sample Vr1a).

Sample L82-2 from the staurolite–chlorite zone

The foliation S_{1-2} is defined by oriented muscovite, abundant chlorite, rare biotite, and ilmenite and quartz (Fig. 3a). Accessory phases include zircon, apatite and one inclusion of allanite found in garnet, and zircon and apatite in the matrix. Porphyroblasts of staurolite are small (1 mm) and garnet (~2 mm) contains curved S_1 inclusion trails of quartz and ilmenite indicating its syntectonic growth. Garnet shows strong zoning marked by a

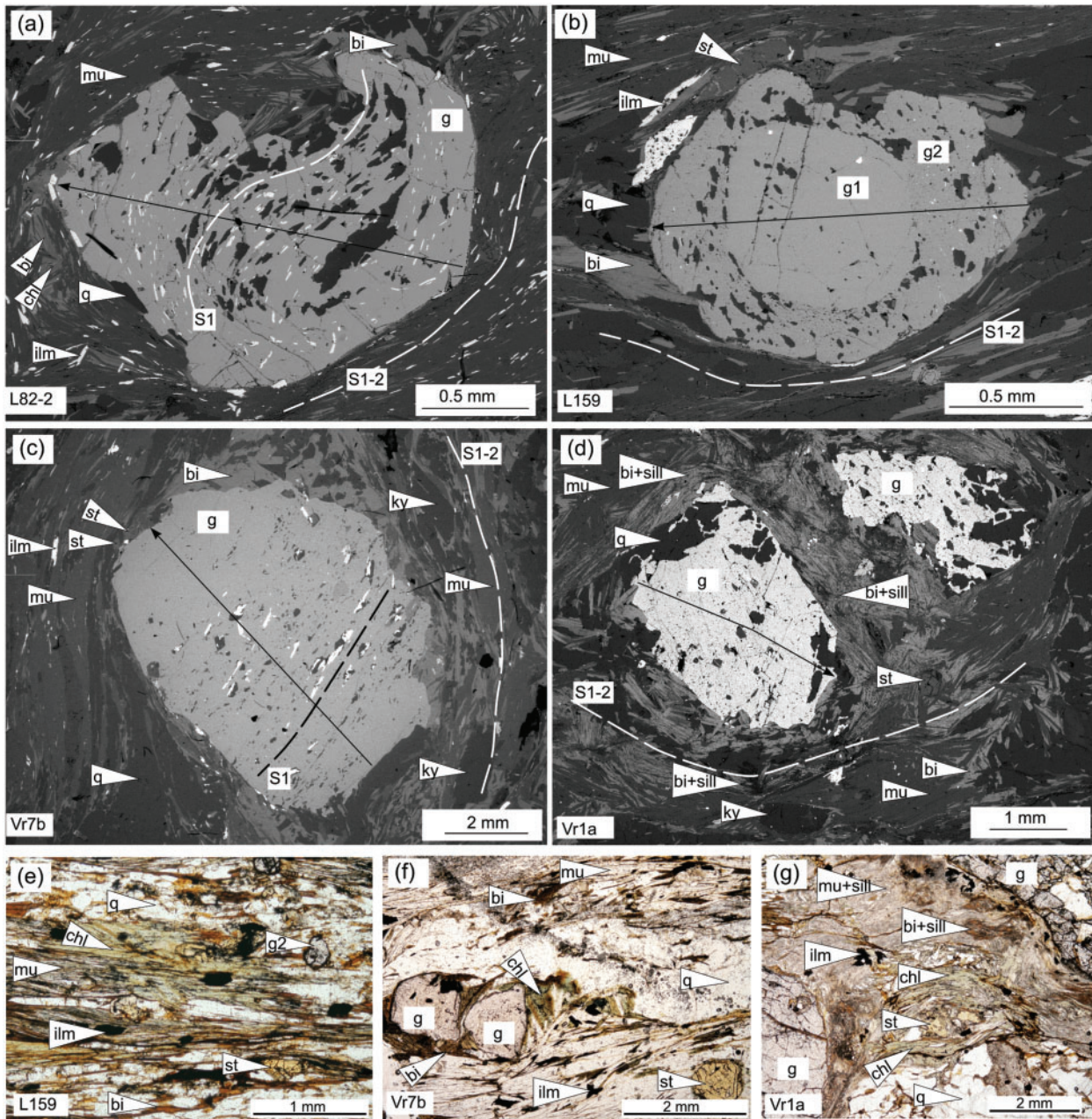


Fig. 3. Backscattered electron images and photomicrographs of typical mineral assemblages and crystallization–deformation relations in the various zones. Arrows indicate profiles across garnet shown in Fig. 4. (a) Sample L82-2. Spiral inclusion trails S_1 of ilmenite and quartz in garnet indicate syntectonic garnet growth. Matrix with S_{1-2} fabric is formed by muscovite, chlorite, biotite, quartz and ilmenite with staurolite (not shown). (b) Sample L159. Two-stage garnet; matrix formed of muscovite, biotite, quartz and ilmenite. (c) Sample Vr7b. Straight inclusion trails S_1 in garnet marked by ilmenite and quartz, and by included staurolite, kyanite and rutile. Matrix assemblage of muscovite, biotite, staurolite, kyanite, ilmenite and rutile in S_{1-2} foliation. (d) Sample Vr1a. Garnet surrounded by a moat of sillimanite and biotite aggregates. Staurolite and kyanite occur in the matrix. (e) Sample L159. Chlorite overgrowth on the S_1 foliation. (f) Sample Vr7b. Chlorite in garnet pressure shadow overprinting S_2 fabric. (g) Sample Vr1a. Chlorite around staurolite overprinting S_2 fabric.

continuous decrease in spessartine and increase in almandine, flat pyrope and grossular contents from core to rim, and a decrease in grossular and an increase in pyrope at the rim ($grs_{0.09} \rightarrow 0.06$, $alm_{0.65} \rightarrow 0.74$, $prp_{0.07} \rightarrow 0.09$, $sps_{0.20} \rightarrow 0.12$, $X_{Fe0.90} \rightarrow 0.88$) (Fig. 4). Staurolite X_{Fe} is 0.81–0.85; plagioclase is 27–30% anorthite. Chlorite is aligned in the foliation together with muscovite and biotite, and some has partially replaced biotite; therefore

chlorite is interpreted as part of the peak mineral assemblage as well as a retrograde phase.

Sample L159 from the staurolite zone

The S_{1-2} matrix is composed of oriented biotite, muscovite, ilmenite and recrystallized ribbons of quartz (Fig. 3b) and a little plagioclase. Garnet exhibits two

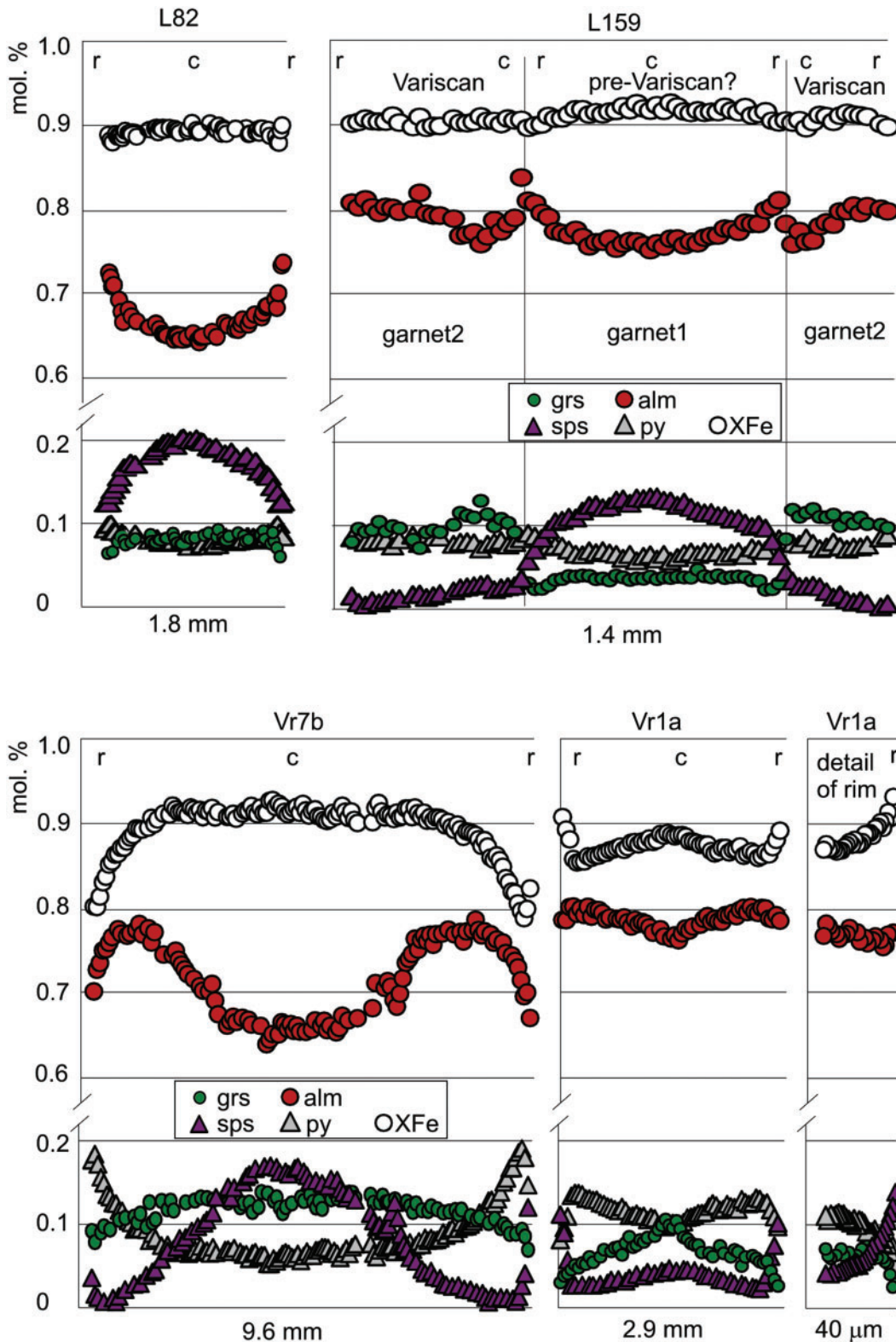


Fig. 4. Garnet zoning profiles; c, core; r, rim. (For location of profiles see Fig. 3.)

stages of growth: 'garnet 1' (1mm) in the inner core with rare inclusions and 'garnet 2' in the rim (0.5mm) with abundant quartz and ilmenite inclusions (Fig. 4). The major chemical difference between these two

generations is high spessartine and low grossular in garnet 1 compared with garnet 2. Garnet 1 shows decreasing spessartine and X_{Fe} , increasing almandine and flat grossular and pyrope from core to rim, with a

Table 1: Representative mineral analyses

Mineral:	garnet	garnet	garnet1	garnet1	garnet2	garnet2	garnet	garnet	garnet	garnet	garnet	garnet
Sample:	L82-c	L82-rim	L159	L159	L159	L159	Vr7b	Vr7b	Vr7b	Vr1a	Vr1a	Vr1a
Position:	core	rim	core	rim	core	rim	core	near rim	rim	core	near rim	rim
SiO ₂	36.27	37.27	35.90	35.97	36.46	36.79	36.49	37.29	37.35	36.91	37.18	36.18
TiO ₂	0.24	0.16	0.20	0.24	0.20	0.15	0.26	0.20	n.d.	0.17	0.16	0.16
Al ₂ O ₃	20.77	21.60	21.03	20.95	21.37	21.50	20.81	21.47	21.67	21.30	21.66	20.94
FeO	28.66	32.30	33.40	35.41	33.92	35.91	28.73	34.64	30.57	33.31	35.87	34.68
MnO	8.76	5.35	5.84	4.38	1.66	0.47	7.48	0.27	5.33	2.71	0.93	5.49
MgO	1.91	2.02	1.59	1.83	2.06	2.31	1.29	3.19	3.70	2.04	2.97	1.92
CaO	2.82	2.01	1.44	0.95	4.25	3.53	4.70	3.51	2.43	4.92	2.39	0.98
Na ₂ O	0.08	0.07	0.05	0.14	0.10	0.12	0.08	0.12	0.04	0.06	0.12	0.06
K ₂ O	0.05	0.05	0.12	0.07	0.04	0.09	0.05	n.d.	0.05	0.06	0.12	0.13
ZnO	n.d.	n.d.	n.d.	n.d.	n.d.	n.d.	n.d.	n.d.	n.d.	n.d.	n.d.	n.d.
Total	99.56	100.83	99.57	99.94	100.06	100.87	99.89	100.69	101.14	101.48	101.40	100.55
<i>Cations</i>												
Si	2.95	2.99	2.93	2.93	2.93	2.94	2.96	2.97	2.95	2.93	2.95	2.93
Ti	0.01	0.01	0.01	0.01	0.01	0.01	0.02	0.00	n.d.	0.01	0.01	0.01
Al	1.99	2.04	2.03	2.01	2.03	2.02	1.99	2.00	2.02	1.99	2.02	2.00
Fe	1.95	2.17	2.28	2.41	2.28	2.40	1.95	2.36	2.02	2.21	2.38	2.35
Mn	0.60	0.36	0.40	0.30	0.11	0.03	0.51	0.04	0.36	0.18	0.06	0.38
Mg	0.23	0.24	0.19	0.22	0.25	0.27	0.16	0.31	0.44	0.24	0.35	0.23
Ca	0.25	0.17	0.13	0.08	0.37	0.30	0.41	0.30	0.21	0.42	0.20	0.08
Na	0.01	0.01	0.01	0.02	0.02	0.02	0.01	0.01	0.01	0.01	0.02	0.01
K	0.01	0.01	0.01	0.01	0.00	0.01	0.00	n.d.	0.00	0.01	0.01	0.01
Zn	n.d.	n.d.	n.d.	n.d.	n.d.	n.d.	n.d.	n.d.	n.d.	n.d.	n.d.	n.d.
Total	8.00	8.00	8.00	8.00	8.00	8.00	8.00	8.00	8.00	8.00	8.00	8.00
X _{Fe}	0.89	0.90	0.92	0.92	0.90	0.90	0.93	0.89	0.82	0.90	0.87	0.91
alm	0.64	0.74	0.76	0.80	0.76	0.80	0.64	0.79	0.67	0.72	0.79	0.77
prp	0.08	0.08	0.06	0.07	0.08	0.09	0.05	0.10	0.14	0.08	0.12	0.08
sps	0.20	0.12	0.13	0.10	0.04	0.01	0.17	0.01	0.12	0.06	0.02	0.12
grs	0.08	0.06	0.04	0.03	0.12	0.10	0.13	0.10	0.07	0.14	0.07	0.03

Mineral:	staurolite	staurolite	staurolite	staurolite	staurolite	staurolite	chlorite	chlorite	chlorite
Sample:	L159-core	L159-rim	Vr7b-core	Vr7b-rim	Vr1a-core	Vr1a-rim	L159	Vr1a	Vr7b
Position:	core	rim	core	rim	core	rim	matrix	matrix	matrix
SiO ₂	27.44	27.39	27.22	27.33	27.88	27.10	24.14	24.07	24.63
TiO ₂	0.48	0.62	0.53	0.52	0.75	0.69	0.10	0.14	0.15
Al ₂ O ₃	53.78	54.03	52.42	54.01	53.85	54.10	23.02	22.13	21.61
FeO	13.69	13.29	13.44	13.00	12.31	12.80	26.99	26.61	23.35
MnO	n.d.	n.d.	0.55	0.49	0.20	0.30	n.d.	0.20	0.25
MgO	1.24	1.10	1.64	1.30	1.11	1.10	12.96	12.64	15.43
CaO	n.d.	n.d.	n.d.	n.d.	n.d.	n.d.	n.d.	n.d.	n.d.
Na ₂ O	n.d.	n.d.	n.d.	n.d.	n.d.	n.d.	n.d.	n.d.	n.d.
K ₂ O	n.d.	n.d.	n.d.	n.d.	n.d.	n.d.	n.d.	n.d.	n.d.
ZnO	0.83	0.83	0.61	1.01	0.38	0.33	n.d.	n.d.	n.d.
Total	97.46	97.26	96.41	97.66	96.48	96.43	87.21	85.80	85.42
<i>Cations</i>									
Si	3.92	3.92	3.93	3.89	4.01	3.90	5.18	5.26	5.30
Ti	0.05	0.07	0.06	0.06	0.08	0.07	0.02	0.02	0.02
Al	9.05	9.11	8.91	9.06	9.13	9.18	5.82	5.70	5.48
Fe	1.63	1.59	1.62	1.55	1.48	1.54	4.84	4.86	4.20
Mn	n.d.	n.d.	0.07	0.06	0.02	0.04	n.d.	0.04	0.05
Mg	0.26	0.23	0.35	0.28	0.24	0.24	4.14	4.12	4.95
Ca	n.d.	n.d.	n.d.	n.d.	n.d.	n.d.	n.d.	n.d.	n.d.
Na	n.d.	n.d.	n.d.	n.d.	n.d.	n.d.	n.d.	n.d.	n.d.
K	n.d.	n.d.	n.d.	n.d.	n.d.	n.d.	n.d.	n.d.	n.d.
Zn	0.09	0.09	0.06	0.11	0.04	0.04	n.d.	n.d.	n.d.
Total	15.00	15.00	15.00	15.00	15.00	15.00	20.00	20.00	20.00
X _{Fe}	0.86	0.87	0.82	0.85	0.86	0.87	0.54	0.54	0.46

(continued)

grossular decrease and pyrope increase at the very rim (grs_{0.06} → 0.03, alm_{0.75} → 0.82, prp_{0.06} → 0.08, sps_{0.14} → 0.05, X_{Fe} 0.92 → 0.88). Garnet 2 shows decreasing spessartine, increasing almandine, irregular or decreasing grossular, and flat pyrope and X_{Fe} from core to rim (grs_{0.12} → 0.08, alm_{0.75} → 0.81, prp_{0.08–0.09}, sps_{0.05} → 0.00, X_{Fe} 0.90). Staurolite (0.5 mm) is also oriented parallel to the S_{1–2}

foliation; X_{Fe} is 0.83–0.87. Plagioclase is 14–18% anorthite. Chlorite is rare, aligned in the foliation where it replaces biotite or it has statically overgrown the S_{1–2} foliation (Fig. 3e). It is therefore interpreted as a retrograde phase. Accessory zircon is included in garnet 1 and 2 and occurs in matrix, whereas apatite and monazite are observed in garnet 2 and the matrix only.

Table 1: Continued

Mineral: Sample:	biotite L159	biotite Vr7b	biotite Vr1a	muscovite L159	muscovite Vr7b	muscovite Vr1a	plagioclase L159	plagioclase Vr7b	plagioclase Vr1a
SiO ₂	35.31	35.17	35.02	46.15	45.20	45.45	65.14	63.58	65.00
TiO ₂	1.75	2.15	2.35	0.38	0.59	0.73	0.00	0.00	0.00
Al ₂ O ₃	19.36	18.63	18.83	36.82	33.47	35.15	22.26	23.10	21.75
FeO	20.46	19.75	20.42	0.77	3.01	0.87	n.d.	n.d.	n.d.
MnO	n.d.	0.20	n.d.	n.d.	n.d.	n.d.	n.d.	n.d.	n.d.
MgO	8.43	9.37	7.99	0.39	0.62	0.56	n.d.	n.d.	n.d.
CaO	n.d.	n.d.	n.d.	n.d.	n.d.	0.03	3.17	4.13	2.67
Na ₂ O	0.31	0.27	0.24	2.01	1.17	1.19	9.82	9.30	10.07
K ₂ O	8.54	9.47	9.06	8.25	9.62	9.44	n.d.	n.d.	0.02
ZnO	n.d.	n.d.	n.d.	n.d.	n.d.	n.d.	n.d.	n.d.	n.d.
Total	94.16	95.00	93.91	94.76	93.69	93.43	100.38	100.11	99.51
<i>Cations</i>									
Si	2.81	2.76	2.80	3.06	3.07	3.08	2.86	2.81	2.87
Ti	0.10	0.13	0.14	0.02	0.03	0.04	0.00	0.00	0.00
Al	1.81	1.72	1.78	2.88	2.68	2.81	1.15	1.20	1.13
Fe	1.36	1.30	1.37	0.04	0.17	0.05	n.d.	n.d.	n.d.
Mn	n.d.	0.01	n.d.	n.d.	n.d.	n.d.	n.d.	n.d.	n.d.
Mg	1.00	1.09	0.95	0.04	0.06	0.06	n.d.	n.d.	n.d.
Ca	n.d.	n.d.	n.d.	n.d.	n.d.	0.00	0.15	0.20	0.13
Na	0.05	0.04	0.04	0.26	0.15	0.16	0.84	0.80	0.86
K	0.87	0.95	0.92	0.70	0.83	0.82	n.d.	n.d.	0.00
Zn	n.d.	n.d.	n.d.	n.d.	n.d.	n.d.	n.d.	n.d.	n.d.
Total	8.00	8.00	8.00	7.00	7.00	7.00	5.00	5.00	5.00
X _{Fe}	0.58	0.54	0.59						
						ab	0.85	0.80	0.87
						an	0.15	0.20	0.13
						or	0.00	0.00	0.00

b.d., below detection, alm = Fe/(Ca + Fe + Mg + Mn), prp = Mg/(Ca + Fe + Mg + Mn), grs = Ca/(Ca + Fe + Mg + Mn), sps = Mn/(Ca + Fe + Mg + Mn), X_{Fe} = Fe/(Fe + Mg), an = Ca/(Na + Ca + K), ab = Na/(Na + Ca + K), or = K/(Na + Ca + K).

Sample Vr7b from the kyanite zone

The matrix, composed of oriented muscovite, biotite, ilmenite, rutile, recrystallized quartz ribbons and plagioclase, contains preferentially oriented porphyroblasts of staurolite and kyanite parallel to the S₁₋₂ foliation (Fig. 3c). Accessory phases include zircon and monazite in garnet, staurolite and the matrix; apatite is present in garnet and the matrix. Garnet porphyroblasts with straight or curved S₁ inclusion trails marked by ilmenite, rutile, quartz and rare staurolite and kyanite indicate garnet growth in the same S₁ foliation as the matrix minerals and rotation during growth. The crystallization–deformation relationships suggest re-folding and reactivation of the matrix into a composite S₁₋₂ foliation. Garnet is strongly zoned with decreasing spessartine, grossular and X_{Fe}, and increasing almandine and pyrope from core towards the rim. At the rim, spessartine increases, pyrope, almandine and grossular decrease, and X_{Fe} increases (grs_{0.14} → 0.09 → 0.08, alm_{0.65} → 0.79 → 0.68, prp_{0.06} → 0.20, sps_{0.28} → 0.00 → 0.12, X_{Fe} 0.90 → 0.78 → 0.83) (Fig. 4). Staurolite X_{Fe} is 0.81–0.85; plagioclase is 14–28% anorthite. Chlorite is very rare, occurs in garnet pressure shadows and is therefore interpreted as retrograde and related to the D₃ event (Fig. 3f).

Sample Vr1a from the kyanite–sillimanite zone

The foliation S₁₋₂ is defined by oriented muscovite, biotite, ilmenite and recrystallized ribbons of quartz and plagioclase, and surrounds porphyroblasts of staurolite

and kyanite. Sillimanite is associated with biotite aligned in the matrix. Abundant sillimanite–biotite aggregates form pressure shadows and thick coronas around garnet and are interpreted as reaction products consuming garnet during the D₂ deformation phase (Fig. 3d). Accessory phases are zircon, monazite and apatite, present in garnet and the matrix; kyanite contains inclusions of zircon and monazite only. Garnet is zoned with decreasing spessartine, grossular, X_{Fe} and increasing pyrope and almandine from core towards rim; the rim is characterized by increasing spessartine and X_{Fe}, decreasing grossular, pyrope and almandine (grs_{0.10} → 0.05 → 0.03, alm_{0.76} → 0.81 → 0.76, prp_{0.10} → 0.14 → 0.05, sps_{0.05} → 0.03 → 0.15, X_{Fe} 0.89 → 0.85 → 0.93) (Fig. 4). Staurolite X_{Fe} is 0.82–0.89, plagioclase is 10–14% anorthite. Chlorite is very rare, occurs around garnet and staurolite, and is therefore interpreted as retrograde and related to the D₃ deformation event (Fig. 3g).

MINERAL EQUILIBRIA MODELLING

Calculation methods

Pseudosections were calculated using Perplex (Connolly, 2005, version Perple_X 07) with dataset 5.5 (Holland & Powell, 1998, November 2003 upgrade), in the system MnO–Na₂O–CaO–K₂O–FeO–MgO–Al₂O₃–SiO₂–H₂O–TiO₂–O (MnNCKFMASHTO). The following activity models were used: Mn-bearing models for chloritoid, staurolite and cordierite are a combination of

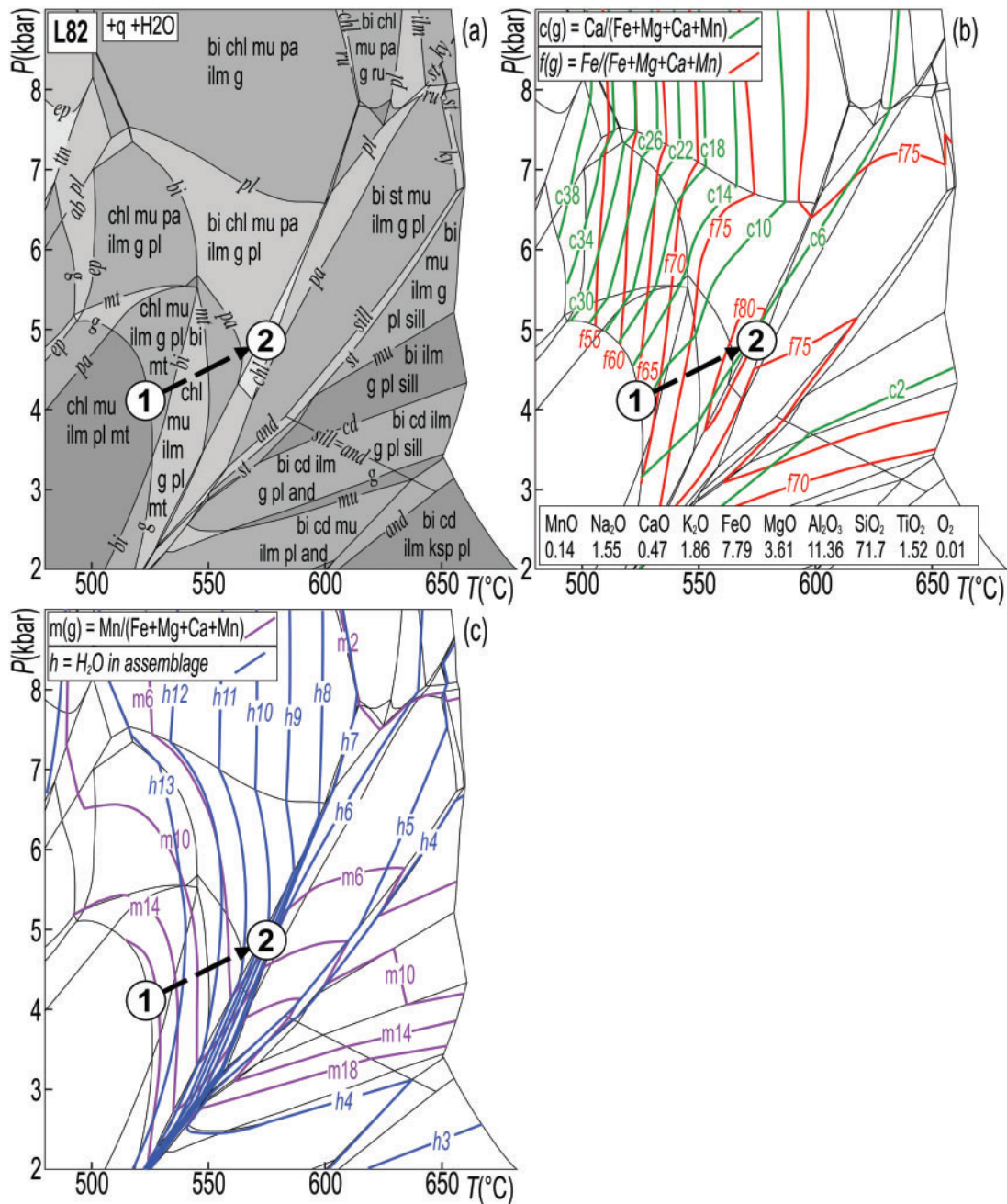


Fig. 5. Pseudosections for samples L82 (a–c) and L159 (d–i) with P – T conditions and P – T paths inferred from the mineral assemblage and garnet composition. (d–f) Pseudosection calculated with uncorrected whole-rock composition for sample L159; the ellipse indicates the P – T range compatible with the composition of garnet 1. (g–i) Pseudosection for sample L159 calculated with 1.1 mol % of garnet 1 subtracted. The isopleth notation used is: $f(g) = \text{Fe}/(\text{Ca} + \text{Fe} + \text{Mg} + \text{Mn}) \times 100$; $c(g) = \text{Ca}/(\text{Ca} + \text{Fe} + \text{Mg} + \text{Mn}) \times 100$; $m(g) = \text{Mn}/(\text{Ca} + \text{Fe} + \text{Mg} + \text{Mn}) \times 100$; $h = \text{mol \% of H}_2\text{O bound in the mineral assemblage}$. (See text for details.)

formulations by Mahar *et al.* (1997) and Holland & Powell (1998), Mn-bearing chlorite is a combination of formulations by Mahar *et al.* (1997) and Holland *et al.* (1998), garnet is from White *et al.* (2000), biotite and sillicate melt from White *et al.* (2007), muscovite and paragonite from Coggon & Holland (2002), plagioclase and K-feldspar from Holland & Powell (2003), and epidote from Holland & Powell (1998). Ilmenite is considered to be an ideal solution of Fe–Mg–Mn endmembers.

Titanite, magnetite, rutile, kyanite, sillimanite, andalusite and quartz are considered pure endmembers.

Whole-rock compositions were obtained using standard wet chemical methods. The whole-rock compositions are indicated on the pseudosections in molar per cent normalized to 100%. H_2O is set in excess. Mineral composition isopleths are shown for the phases of interest—especially to study garnet growth and zoning to infer prograde P – T trajectories. The

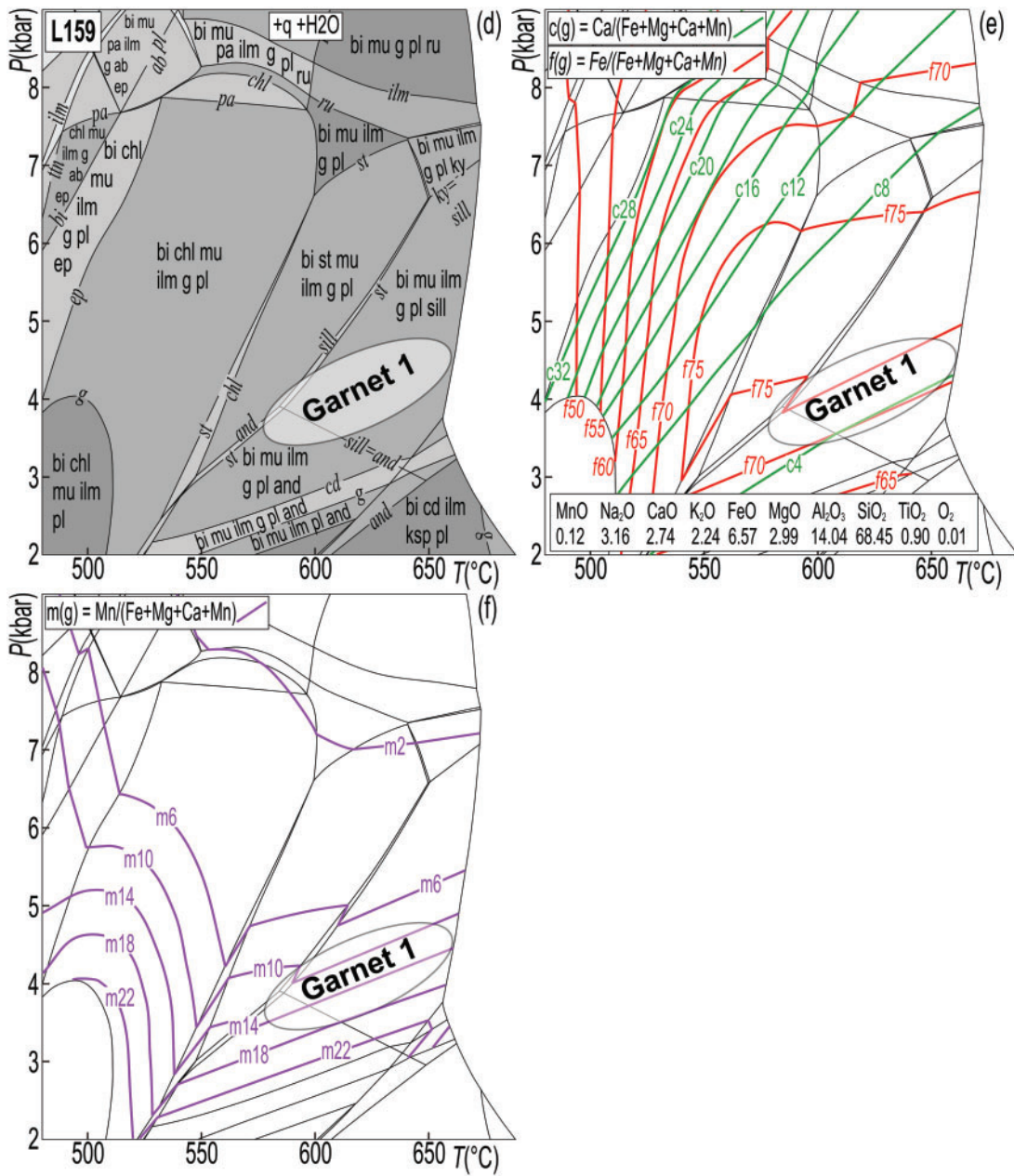


Fig. 5. Continued

pseudosections are also contoured with crystal-bound H₂O content to determine whether the rocks were likely to have released or consumed H₂O along the inferred P–T path.

P–T paths

Pseudosection for sample L82-2 from the staurolite–chlorite zone

The matrix assemblage bi–chl–mu–g–st–ilm–pl is compatible with the field bi–chl–mu–g–st–ilm–pl ± pa in the pseudosection (Figs 3a and 5a–c). Garnet zoning (grs_{0.09} → 0.06, alm_{0.65} → 0.74, prp_{0.07} → 0.09, sps_{0.20} → 0.12, X_{Fe} 0.90 → 0.88) constrains the beginning of garnet growth

at the garnet-in line at ~520°C and 4 kbar (point 1, Fig. 5a–c) and the end of garnet growth at ~570°C and 5 kbar (point 2, Fig. 5a–c).

Pseudosection for sample L159 from the staurolite zone

For sample L159, garnet 1 generation is presumed to have formed in a pre-Variscan event and therefore the first pseudosection was calculated for the measured whole-rock composition to estimate the P–T conditions of garnet 1 formation and its molar proportion (Fig. 5d–f). An adequate amount of garnet estimated from the calculations (1.1 mol %) was then subtracted from the whole-rock composition to obtain an effective

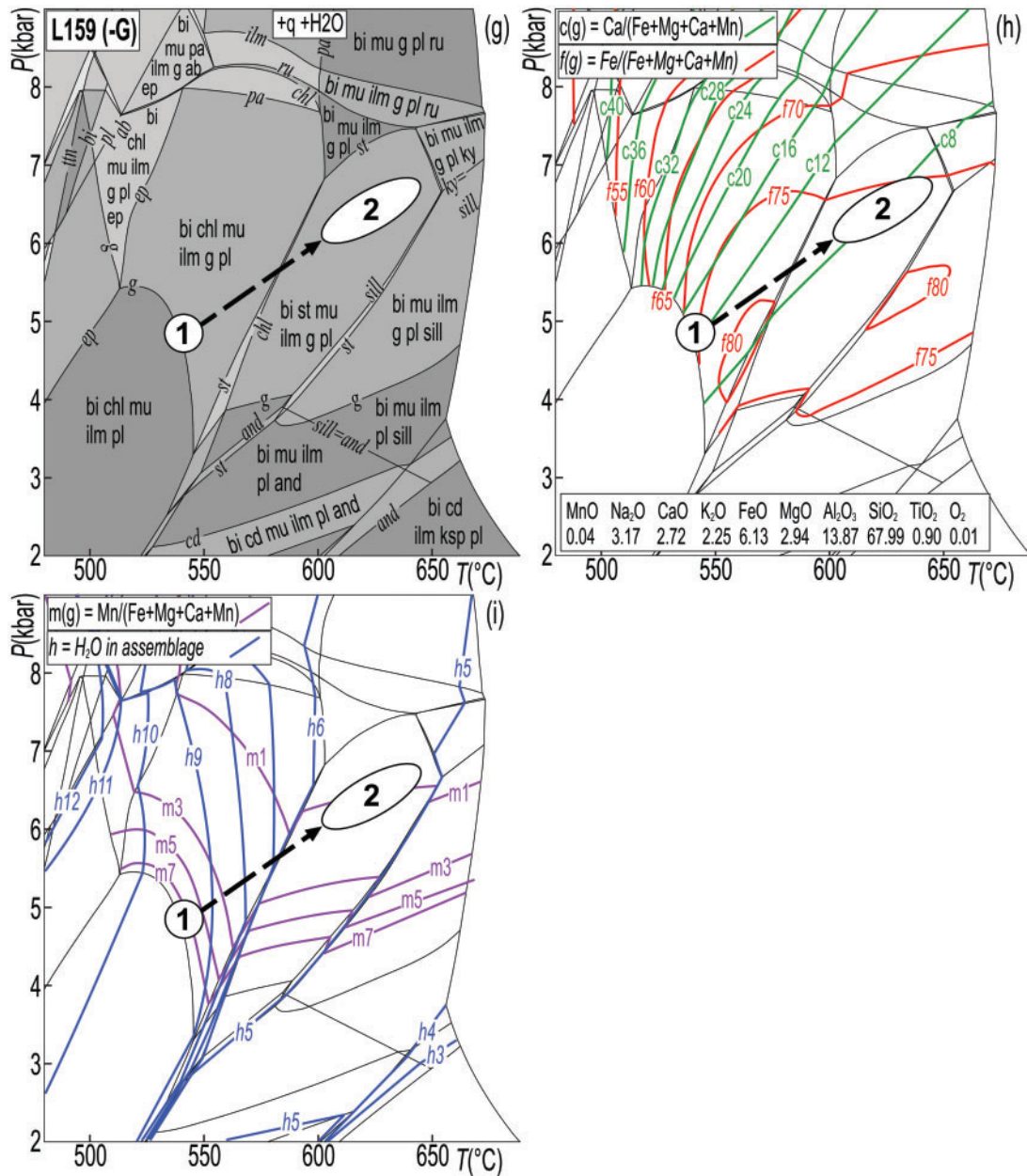


Fig. 5. Continued

whole-rock composition for modelling of the equilibria corresponding to garnet 2 formation and the matrix assemblage (Fig. 5g–i).

Garnet 1 mineral chemistry in the pseudosection for the uncorrected bulk-rock composition matches the calculated isopleths in the range 3–5 kbar and 550–650°C (Fig. 5d–f). The rock dehydrated during the event producing garnet 1; however, because the chemistry of the garnet 2 core coincides with the garnet-in line in the H₂O-saturated pseudosection (Fig. 5d–f), it is likely that the rock evolved at least from these *P*–*T* conditions again as H₂O-saturated. In the pseudosection for the bulk-rock composition corrected for 1.1% of garnet 1 (Fig. 5g–i), the matrix assemblage bi–mu–g–st–ilm–pl is compatible with the field bi–mu–g–st–ilm–pl (Figs 3b

and 5g–i). Garnet 2 zoning ($\text{grs}_{0.12} - 0.08$, $\text{alm}_{0.75} - 0.81$, $\text{prp}_{0.08-0.09}$, $\text{sps}_{0.05} - 0.00$, $X_{\text{Fe}} 0.90$) constrains the beginning of garnet growth to ~540°C and 4–9 kbar (point 1, Fig. 5g–i) and the end of garnet growth to ~600–640°C and 6–7 kbar (point 2, Fig. 5g–i). Retrograde chlorite (Fig. 3e) indicates crossing of the chlorite-in reaction at 550–570°C.

Pseudosection for sample Vr7b from the kyanite zone

Minerals in the matrix and inclusions in garnet are compatible with a *P*–*T* path passing through the staurolite-in line, the ilmenite–rutile transition, and the ky-in line into the bi–st–mu–g–ky–ru–pl field (Figs 3c and 6a–c). As this

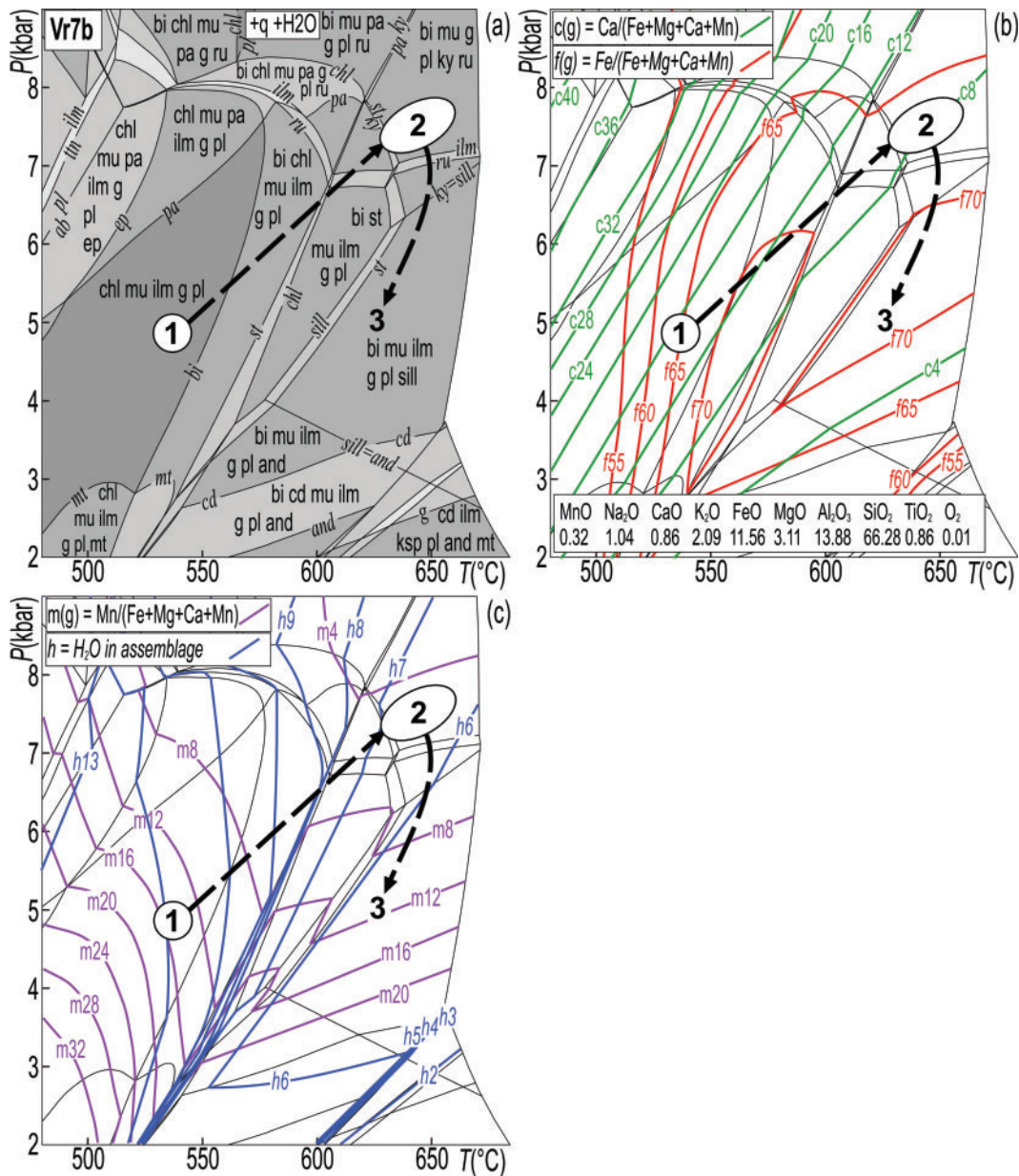


Fig. 6. Pseudosections for sample Vr7b (a–c) and sample Vr1a (d–f). *P*–*T* paths are inferred from the mineral assemblage and garnet composition. (See text for details.)

field is small, it is likely that the *P*–*T* path continued slightly beyond the calculated staurolite stability. The garnet core composition ($grs_{0.14} \rightarrow 0.09 \rightarrow 0.08$, $alm_{0.65} \rightarrow 0.79 \rightarrow 0.68$, $prp_{0.06} \rightarrow 0.20$, $spss_{0.28} \rightarrow 0.00 \rightarrow 0.12$, $X_{Fe} 0.90 \rightarrow 0.78 \rightarrow 0.83$) is in agreement with the crossing of isopleths at ~540°C and 4.5 kbar, and the compositional trend in the garnet mantle with growth along a *P*–*T* path heading to 630–650°C and 7.5–8 kbar. The rim ($spss = 12$) is interpreted as having been diffusively modified during decompression; the rim composition of garnet grown at the peak is not preserved. The decompression probably occurred within the sillimanite stability field as indicated by the decrease in grossular and increase in spessartine. Rare retrograde chlorite (Fig. 3f) indicates crossing of the chlorite line at 550–570°C.

Pseudosection for sample Vr1a from the kyanite–sillimanite zone

The presence of staurolite and kyanite indicate peak *P*–*T* conditions in the bi–st–mu–ilm–g–pl–ky field (Figs 3d and 6). Sillimanite–biotite aggregates replacing garnet indicate decompression into the bi–mu–ilm–g–pl–sill field. Garnet zoning ($grs_{0.10} \rightarrow 0.05 \rightarrow 0.03$, $alm_{0.76} \rightarrow 0.81 \rightarrow 0.76$, $prp_{0.10} \rightarrow 0.14 \rightarrow 0.05$, $spss_{0.05} \rightarrow 0.03 \rightarrow 0.15$, $X_{Fe} 0.89 \rightarrow 0.85 \rightarrow 0.93$) is compatible with such a prograde path, followed by decompression. The garnet core composition approximately fits the isopleths at 6 kbar and 550°C with a trend toward 8 kbar and 650°C. However, this trend is only approximate because the peak garnet rim was replaced by sillimanite and biotite. Also, the measured garnet core composition does not fit the

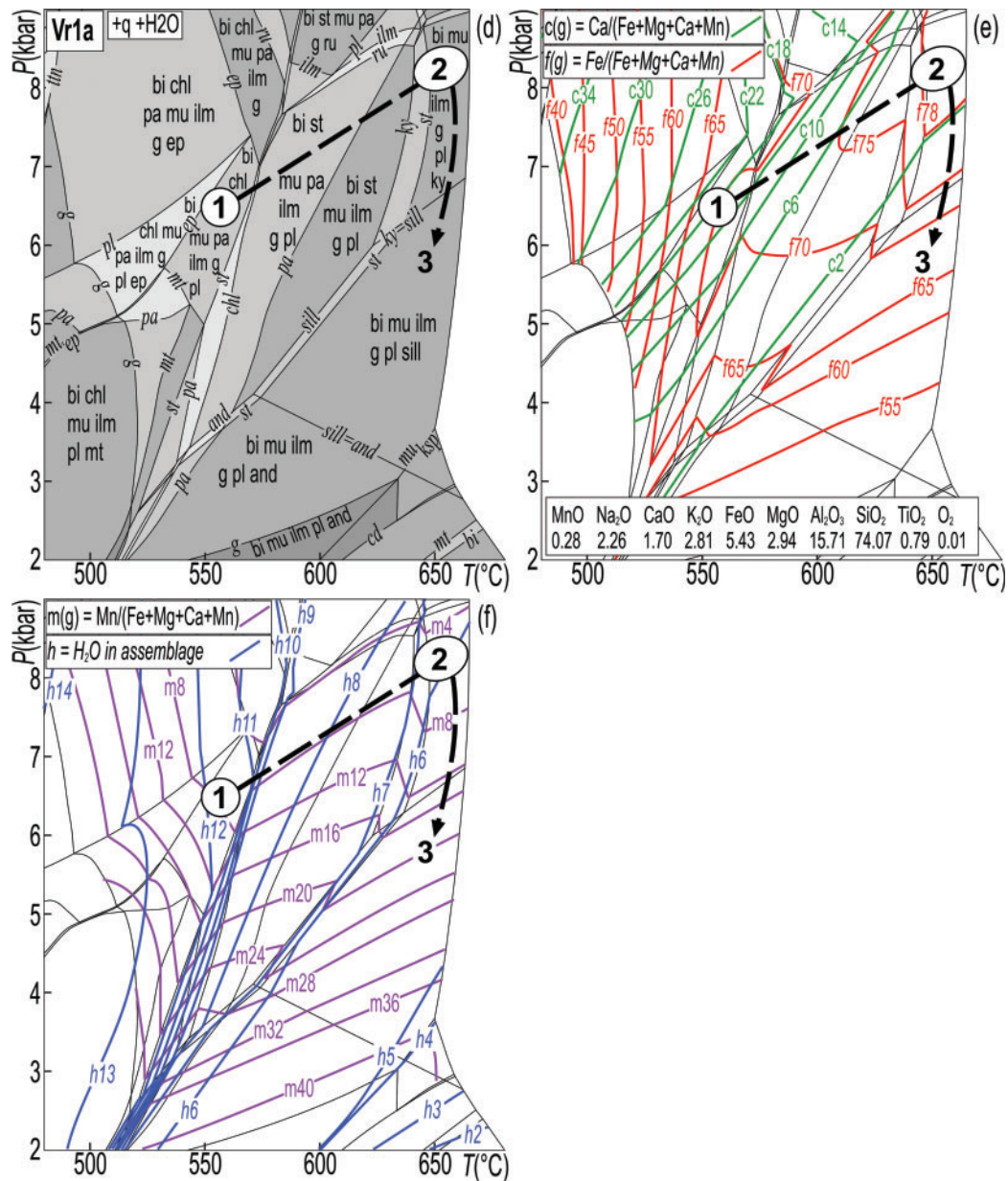


Fig. 6. Continued

isopleths at the garnet-in line—perhaps because the garnet was not cut through the core or because the profile was diffusively flattened. Rare retrograde chlorite indicates crossing of the chlorite line at 550–560°C.

MONAZITE GEOCHRONOLOGY AND TRACE-ELEMENT CHEMISTRY

Methods and sample preparation

Monazite U/Th–Pb and REE data were acquired at the Department of Earth Science, University of California, Santa Barbara, via LASS, allowing simultaneous isotopic and elemental analysis from the same volume of mineral. The analytical procedure followed methods described by Kylander-Clark *et al.* (2013). Samples were ablated in thin

section using a Photon Machines 193 nm ArF excimer ultraviolet laser with a HelEx ablation cell coupled to a Nu Instruments Plasma high-resolution multi-collector inductively coupled plasma mass spectrometry (MC-ICP-MS) system and a Nu Instruments AttoM single-collector ICP-MS system. The laser spot diameter was 10 µm and the laser fluence was ~1 J cm⁻². The laser was fired twice to remove common Pb from the sample surface and this material was allowed to wash out for 10 s. Material was then ablated at 3 Hz for 20 s, resulting in a pit depth of ~8 µm. Masses ²⁰⁴Pb + Hg, ²⁰⁶Pb, ²⁰⁷Pb, and ²⁰⁸Pb were measured on ion counters, and masses ²³²Th and ²³⁸U were measured on Faraday detectors. Analyses of unknowns were bracketed by analyses of monazite primary reference materials (RM) 44069 [424.9 ± 0.4 Ma Pb/U

thermal ionization mass spectrometry (TIMS) date; Aleinikoff, 2006]. A secondary monazite reference material, Stern (512.1 ± 1.9 Ma; J. M. Cottle & D. J. Condon, unpublished data), was also included as a monitor of accuracy and returned an age of 509.5 ± 1.8 Ma [95% confidence interval (CI) internal precision] during the single run reported here.

The Iolite plug-in (Paton *et al.*, 2011) for the Wavemetrics Igor Pro software was used to correct measured isotopic ratios for baselines, time-dependent laser-induced inter-element fractionation, plasma-induced fractionation, and instrument drift. Baseline intensities were determined prior to each analysis. The mean and standard error of the measured ratios of the backgrounds and peaks were calculated after rejection of outliers more than 2 standard errors beyond the mean. Long-term analysis shows that this equipment and method are capable of measuring the baseline- and fractionation-corrected $^{206}\text{Pb}/^{238}\text{U}$ of a primary reference material with a long-term precision of $\pm 0.7\%$; the baseline- and fractionation-corrected $^{207}\text{Pb}/^{206}\text{Pb}$ can be measured with a long-term precision of $\pm 0.4\%$.

The $^{238}\text{U}/^{206}\text{Pb}$ and $^{207}\text{Pb}/^{206}\text{Pb}$ isotopic ratios for each analysis were plotted on Tera–Wasserburg diagrams using Isoplot (Ludwig, 2003). For discordant U–Pb ratios we report a ‘207-corrected date’ (Compston *et al.*, 1992) by assuming a Stacey & Kramers (1975) common-Pb value. The uncertainty given for each isotopic ratio or spot date is given at the 95% confidence interval for the in-run uncertainty, assuming a Gaussian distribution of measurement errors. All of the analyses presented in this study were made in a single 2 h period; to assess population statistics, therefore, we use only the in-run uncertainties. Once population statistics have been assessed, the long-term uncertainty and uncertainties in the isotopic ratios of the primary RM and the U decay constants are added; this uncertainty is given in square brackets. The isotopic ratios do not have sufficient spread in U/Pb ratios to define a $^{238}\text{U}/^{206}\text{Pb}$ – $^{207}\text{Pb}/^{206}\text{Pb}$ isochron, therefore the Stacey–Kramers (e.g. Stacey & Kramers, 1975) model for common lead was used to calculate isochrons. The data are provided as [Supplementary Material in Electronic Appendix 1](#) (available for downloading at <http://www.petrology.oxfordjournals.org>).

Prior to analysis, monazite grains were imaged with backscattered electrons (BSE) and secondary electrons (SE) using a Tescan VEGA scanning electron microscope at the Institute of Petrology and Structural Geology (Charles University in Prague). Compositional mapping for Y, La, Th and U was performed on a CAMECA SX-100 at the Institute of Geosciences, Masaryk University (Brno, Czech Republic).

Results

In three samples monazite $>10\ \mu\text{m}$ occurs in the matrix and as inclusions in garnet, staurolite and kyanite. BSE and X-ray maps are shown in [Figs 7 and 8](#); La and Nd

are unzoned and therefore are not shown. A secondary electron image of monazite in Vr7b is shown in [Fig. 9b](#) to illustrate its internal structure. The results of the U–Pb dating are presented in [Fig. 10](#), and REE patterns of monazite are plotted in [Fig. 11](#). The one $4\ \mu\text{m}$ monazite found in sample L82 was not dated.

Monazite in sample L159, staurolite–biotite zone

Five monazite grains were found in the matrix; no monazite is included in garnet or staurolite. Three grains were studied. They have irregular shapes; two are $10\text{--}20\ \mu\text{m}$ in diameter (not shown) and one is $60\ \mu\text{m}$ ([Fig. 7a](#)). X-ray images of the large grain show slight patchy zoning in Th and U, and low Y ([Fig. 7a](#)).

Seven spots in three grains were analyzed by LASS ([Fig. 7a](#)). The data yield a continuum of ^{207}Pb -corrected $^{238}\text{U}/^{206}\text{Pb}$ dates from 341 ± 5 Ma to 328 ± 5 Ma (2σ in-run uncertainties; [Fig. 10a](#)); they do not form a single population (MSWD = 4.3). Instead, the relative probability distributions show two peaks ([Fig. 10a](#)), confirmed by unmixing multicomponent data using Gaussian deconvolution (dates in brackets in [Fig. 10a](#)). Isochrons calculated for these two groups are 340.3 ± 2.8 [7] Ma (MSWD = 0.06, $n = 4$) and 330.7 ± 2.6 [7] Ma (MSWD = 0.87, $n = 3$), in agreement with ages presented below from monazite inclusions in porphyroblasts and matrix monazite in the kyanite and kyanite–sillimanite zone (see below and [Fig. 10b](#) and c). All of the spots have similar REE patterns ([Fig. 11a](#)) and low heavy REE (HREE) concentrations [normalizing values from [Barcheck *et al.* \(2012\)](#)].

Monazite in sample Vr7b, kyanite zone

Numerous monazite grains were found in the matrix; five are included in kyanite; no monazite was found in garnet or staurolite. Five $10\text{--}350\ \mu\text{m}$ grains were studied; some are subhedral and others have irregular shapes ([Fig. 7b](#)). In X-ray images, the grains included in kyanite or matrix biotite show cores with high Y and low Th ([Fig. 7b](#)). Embayments at the rim and around inclusions tend to be low in Y and rich in Th. Grain 191-1 is aligned parallel to the foliation defined by muscovite, biotite and chlorite ([Fig. 9a](#)) and shows patchy zoning with low Y and low Th. In a secondary electron image, this grain shows subgrain boundaries that tend to join in triple junctions, typical of dynamic recrystallization ([Fig. 9b](#) and c).

Thirty-seven spots in six grains were analyzed by LASS ([Fig. 10b](#)). The data yield a continuum of ^{207}Pb -corrected $^{238}\text{U}/^{206}\text{Pb}$ dates from 341 ± 5 Ma to 330 ± 5 Ma (2σ in-run uncertainties) Ma. They do not form a single population (MSWD = 1.6, $n = 37$), so we consider the data from different monazite textures separately. Isotopic ratios for monazite included in kyanite give a ^{207}Pb -corrected $^{238}\text{U}/^{206}\text{Pb}$ age of 337.1 ± 1.2 [7] Ma (MSWD = 0.71, $n = 12$, one rejected). Monazite in biotite gives an equivalent age of 338.3 ± 1.3 [7] Ma (MSWD = 0.62, $n = 11$). Matrix grain 191-1 with patchy

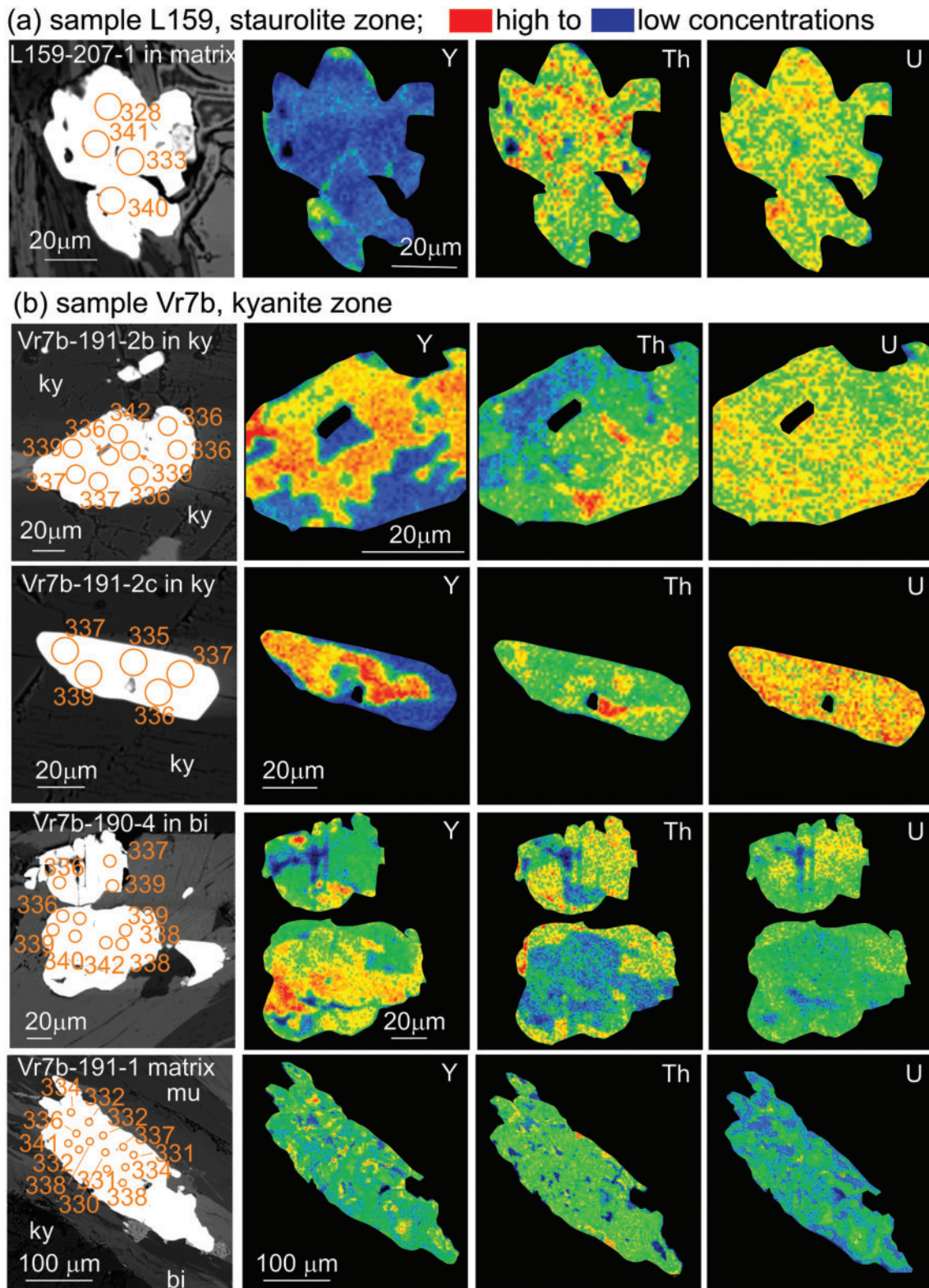


Fig. 7. Backscattered electron (BSE) images and compositional maps of dated monazite grains from samples L159 and Vr7b. The analysis spots are 10 μm in diameter.

zoning shows an asymmetrical probability distribution with a peak at 332 Ma, and a test of unmixing multicomponent data using Gaussian deconvolution (dates in parentheses in Fig. 10b) shows two groups of data. In the

first group, five of the data points from matrix grain 191-1 with patchy zoning yield a similar age of 338.1 ± 2.2 [7] Ma (MSWD = 0.46). For all 28 of these data points we calculate an age of 337.7 ± 0.8 [7] Ma; MSWD = 0.65). In the

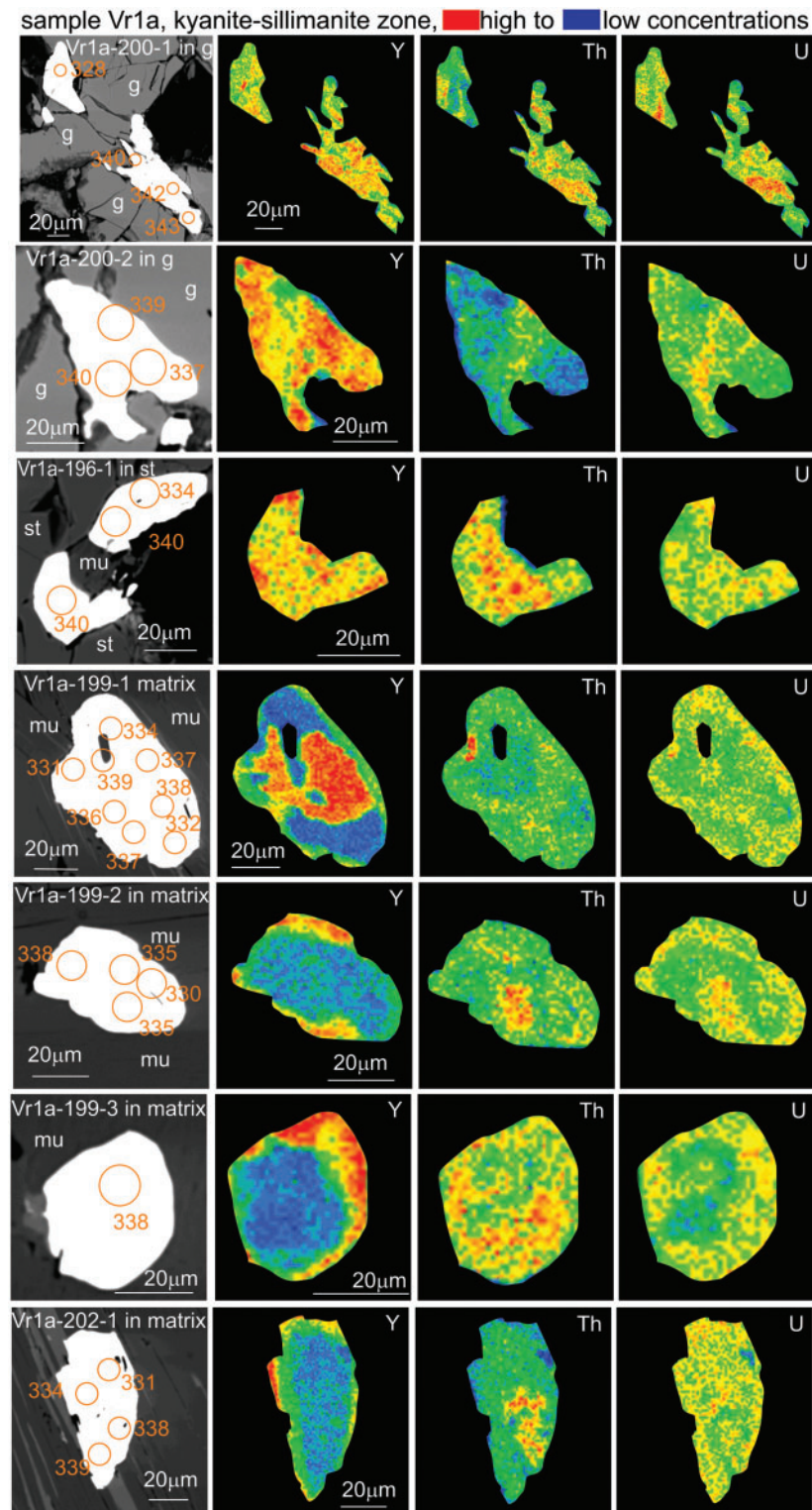


Fig. 8. Backscattered electron (BSE) images and compositional maps of dated monazite grains from sample Vr1a. The analysis spots are 10 μm in diameter.

second group, eight more spots from matrix grain 191-1 with patchy zoning yield an age of 332.0 ± 1.7 [7] Ma (MSWD = 0.27); the in-run uncertainty of 1.7 Ma indicates that this date is significantly younger than the 338–337 Ma monazite in the rock (Fig. 10b).

All of the analyses have slightly elevated HREE concentrations compared with sample L159 (Fig. 11a and b). The analyses from monazite included in kyanite and biotite tend to have higher HREE concentrations compared with monazite from the patchy matrix grain (Fig. 11b).

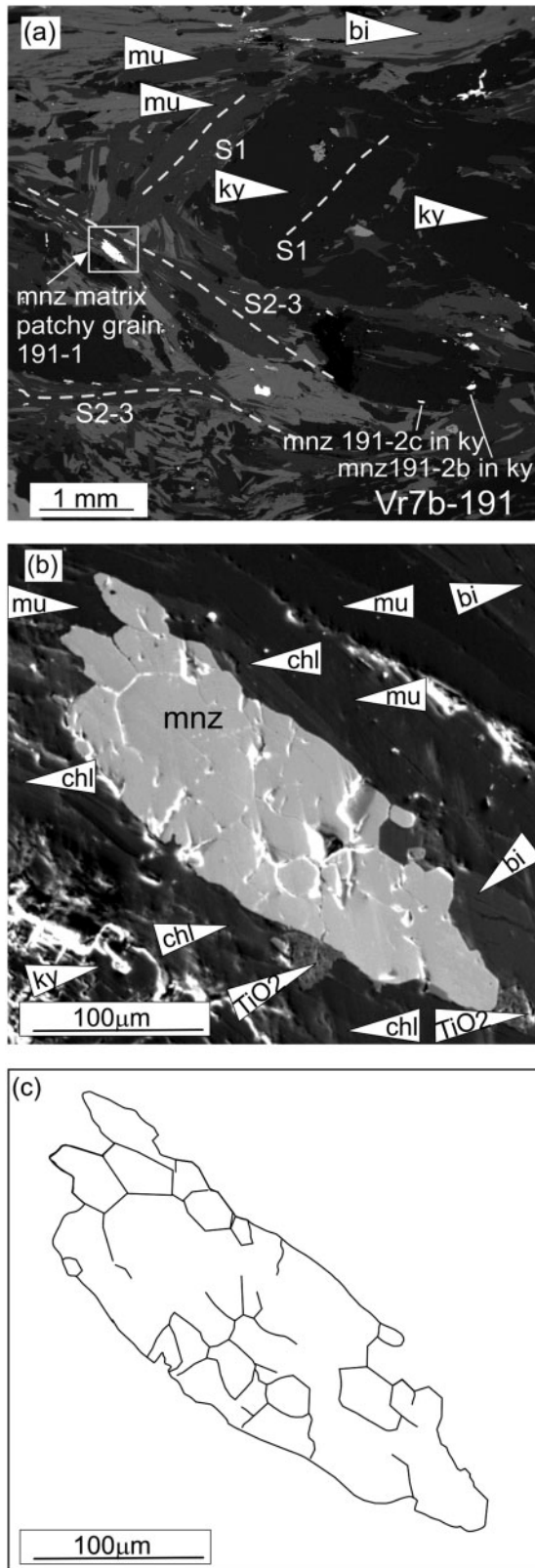


Fig. 9. (a) SEM image showing the position of monazite grain Vr7b-191-1 within the S₂₋₃ fabric, surrounded by muscovite, biotite and chlorite, indicating reactivation of the fabric during the D₃ event. (b, c) Secondary electron image of the monazite and sketch showing an internal structure of straight 'boundaries' that tend to join in triple junctions, typical of dynamic recrystallization processes.

(a) sample L159, staurolite zone

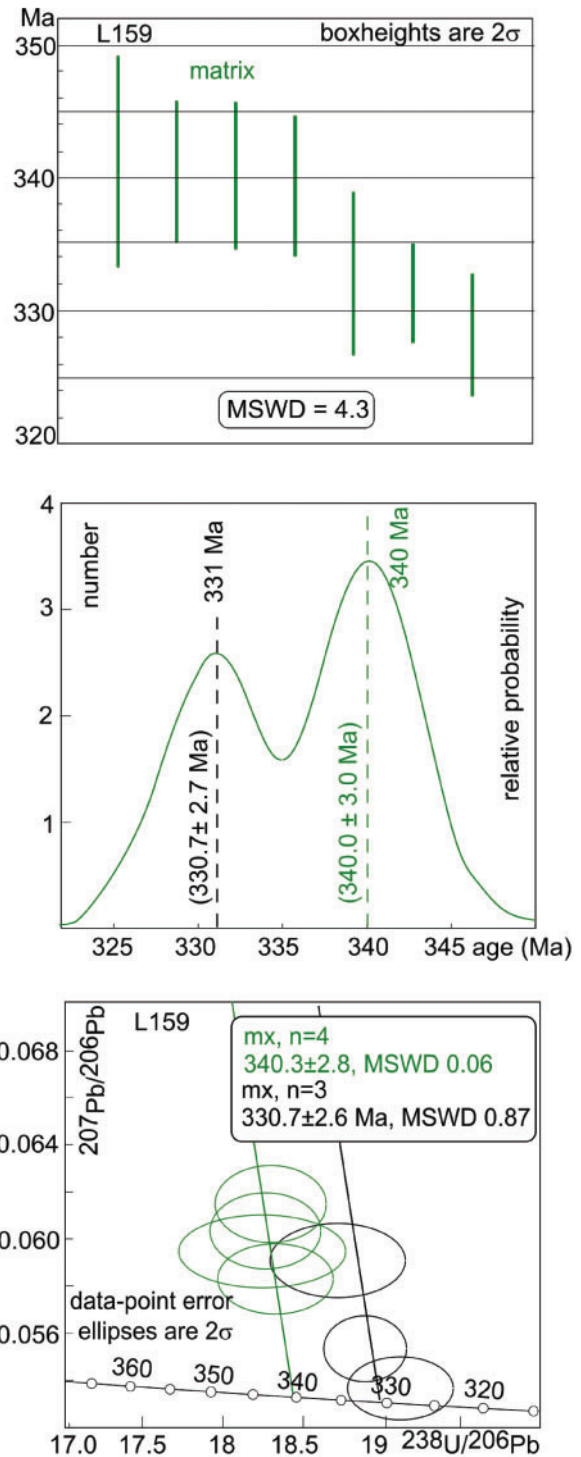


Fig. 10. Monazite LASS results plotted in terms of textural position, a weighted mean probability density plot of ²⁰⁷Pb corrected ²³⁸U/²⁰⁶Pb ages and a Tera-Wasserburg concordia plot. In the probability plot dates indicate positions of peaks; values in parentheses are dates obtained for matrix monazite after performing a test of unmixing multicomponent data using Gaussian deconvolution. The Tera-Wasserburg concordia plots assume a Stacey & Kramers (1975) common-Pb value with 2σ error ellipses. Matrix monazite is divided into two groups after performing a test of unmixing multicomponent data using Gaussian deconvolution. (a) Sample L159; (b) sample Vr7b; (c) sample Vr1a. mx, matrix.

(b) sample Vr7b, kyanite zone

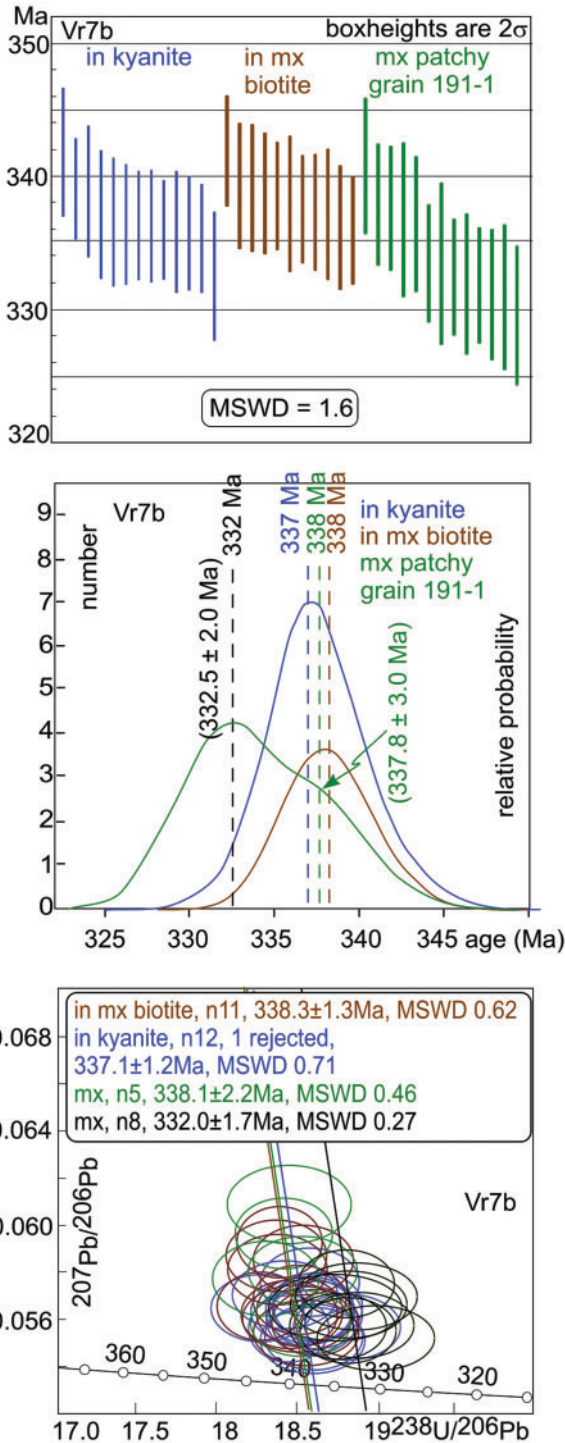


Fig. 10. Continued

The Eu anomaly is positive or negative and shows a large spread, independent of the monazite texture.

Monazite in sample Vr1a, kyanite–sillimanite zone
 Numerous monazite grains were found in the matrix; three monazites are included in garnet, and four in staurolite; no monazite was found in kyanite. Twelve

(c) sample Vr1a, kyanite-sillimanite zone

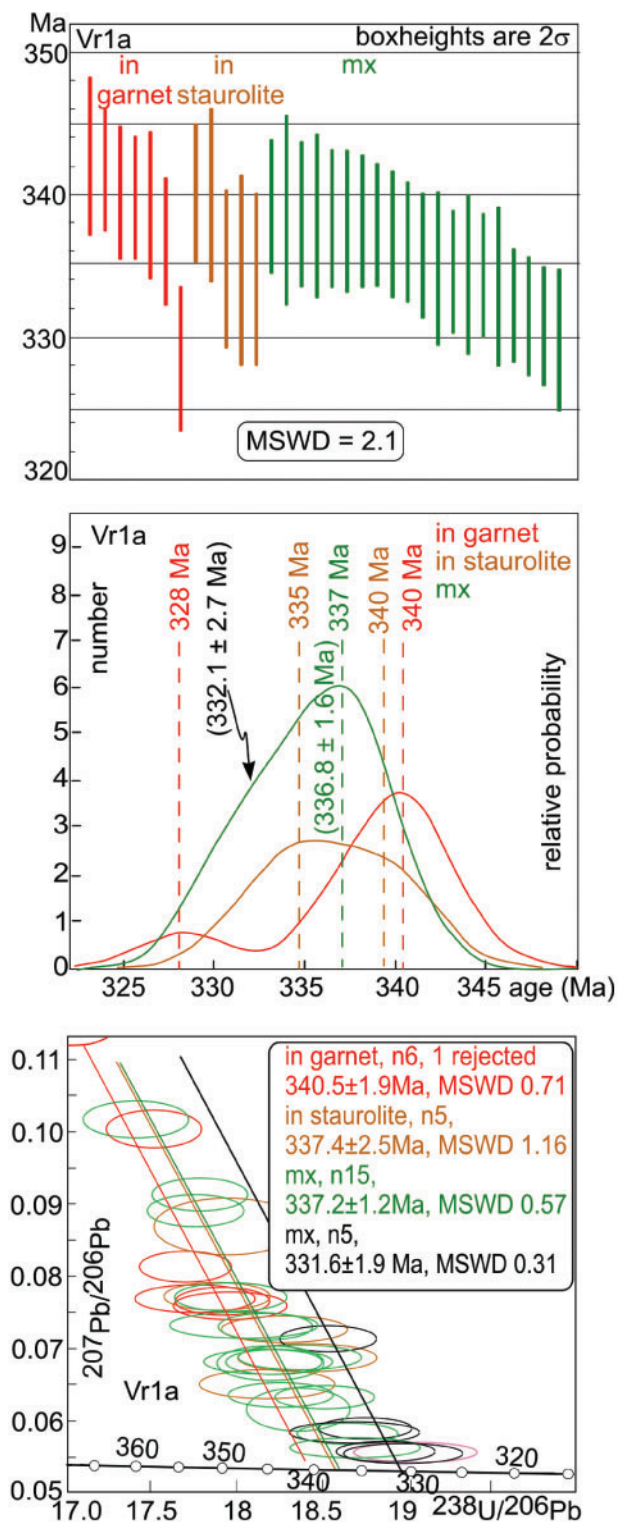


Fig. 10. Continued

20–120 μm grains were studied; some are subhedral whereas others are irregular (Fig. 8). In X-ray images, the grains included in garnet and staurolite have high Y with rim embayments that are lower in Y. Other elements are unzoned, or slightly patchy (Fig. 8). A large

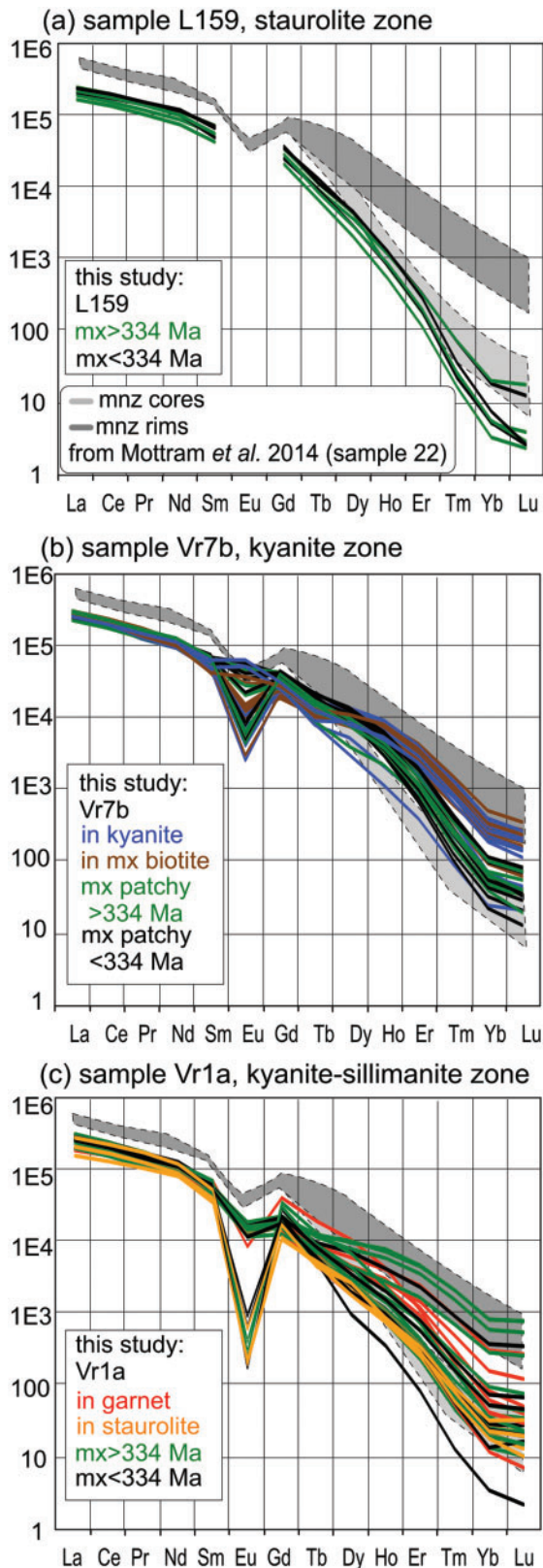


Fig. 11. (a–c) Chondrite-normalized REE patterns of monazite [normalizing values from Barcheck *et al.* (2012)] classified by textural position and compared with the study of Mottram *et al.* (2014). Missing Ce and Eu measurements are due to analytical problems. (d, e) Variation of Yb and Yb/Gd vs age showing an increasing trend with decreasing age from 344 to 335 Ma (black ellipse), then a drop at 335–328 Ma (green ellipse).

matrix grain (Vr1a-199-1 in Fig. 8) has a core with higher Y than the inclusions, a decrease in Y towards the rim and then an increase at the very rim. Some of the zones have sharp boundaries. The other matrix grains have low-Y cores and high-Y rims.

Thirty-two spots in 12 grains were analysed by LASS (Fig. 10c). The data yield a continuum of ^{207}Pb -corrected $^{238}\text{U}/^{206}\text{Pb}$ dates from 343 ± 6 Ma to 328 ± 5 Ma. They do not form a single population (MSWD = 2.1, $n=32$), so we consider the data from different monazite textures separately. Monazite included in garnet yields a ^{207}Pb -corrected $^{238}\text{U}/^{206}\text{Pb}$ isochron age of 340.5 ± 1.9 [7] Ma (MSWD = 0.71, $n=6$, one rejected), and monazite included in staurolite an age of 337.4 ± 2.5 [7] Ma (MSWD = 1.16, $n=5$). Matrix monazite shows an asymmetrical probability distribution of dates, and a test of unmixing multicomponent data using Gaussian deconvolution (dates in parentheses in Fig. 10c) shows two groups of data. In the first group, 15 of the data points from the matrix grains yield a similar age of 337.2 ± 1.2 [7] Ma (MSWD = 0.57). Five more spots from the second group of the matrix grains yield a significantly younger age of 331.6 ± 1.9 [7] Ma (MSWD = 0.31) (Fig. 10c).

The analyses show a considerable spread in HREE concentrations compared with samples L159 and Vr7b (Fig. 11c). The analyses from monazite included in garnet and staurolite and most matrix monazite tend to have low HREE; however, some analyses from matrix grains have increased HREE concentrations. The Eu anomaly ranges from deep to slightly negative.

In summary, the monazite inclusions in garnet, kyanite, staurolite, and biotite in the kyanite and kyanite–sillimanite zone samples are $340 \pm [7]$ Ma to $337 \pm [7]$ Ma. Some matrix monazite is of this age, whereas younger matrix monazite in all three metamorphic zones is 332 – $331 \pm [7]$ Ma. The in-run uncertainties of 1–3 Ma indicate that the 340–337 Ma and 332–331 Ma dates are significantly different (Fig. 10).

DISCUSSION

P–T–d–t paths and the role of H_2O

Combining crystallization–deformation relationships inferred from textures, mineral chemistry and pseudo-section modelling allows us to constrain the prograde and peak conditions for samples from the Parautochthon, Lower Moravian nappe, Upper Moravian nappe and Micaschist zone (Fig. 12). The beginnings of the *P–T* paths are recorded by garnet core compositions at ~ 530 – 540°C and 4–4.5 kbar, except for the Micaschist zone, where the garnet core is interpreted as partially diffusively re-equilibrated or not cut through the core. The peak conditions determined by mineral assemblage and garnet rim (or near rim) composition are $\sim 570^\circ\text{C}$ and 5 kbar for the Parautochthon, ~ 600 – 640°C and 6–7 kbar for the Lower Moravian nappe, and ~ 630 – 650°C and 7.5–8 kbar for the Upper Moravian nappe and the Micaschist zone, in accordance with previous thermobarometric

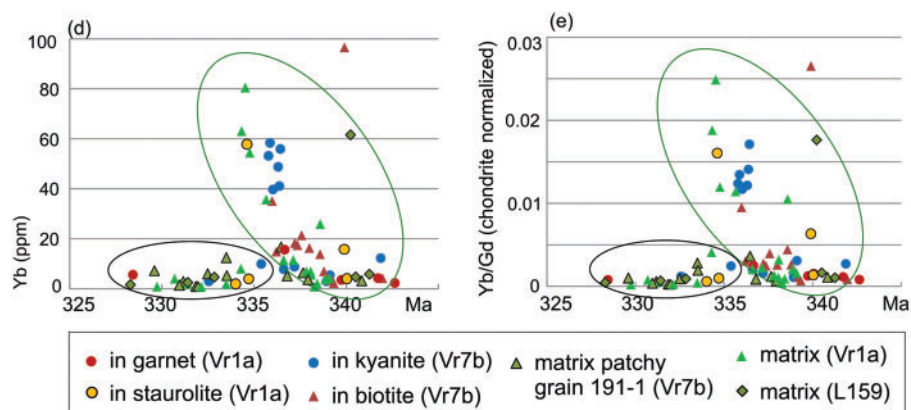


Fig. 11. Continued

estimations (Höck, 1975; Höck *et al.*, 1990; Štípská & Schulmann, 1995). This implies burial during the D₁ event under a similar geothermal gradient, leading to the progressive appearance or disappearance of garnet (-in), staurolite (-in), chlorite (-out) and kyanite (-in). The decompression associated with cooling is documented in the Upper Moravian nappe from garnet rim composition that is interpreted as diffusionally re-equilibrated, and in the Micaschist zone, based on garnet rim composition and the pressure shadows and pseudomorphs of biotite and sillimanite around garnet during deformation event D₂. Further cooling in all units is supported by more or less extensive growth of chlorite, commonly syntectonic with the D₃ deformation event, indicating retrograde crossing of the chlorite (-in) reaction at 560–580°C (Figs 5 and 6); the pressure of this crossing is not constrained, but the absence of cordierite and andalusite indicates >3.5 kbar (Fig. 6). These retrograde conditions are in accordance with conditions of 300°C at 3.3–4 kbar obtained from fluid inclusions in late quartz veins (Fritz & Loitzenbauer, 1994).

The closed- or open-system behavior of H₂O along the retrograde *P–T* path may be evaluated from the observed mineral growth and the bound H₂O contoured in the pseudosections (Figs 5 and 6). During the decompression associated with cooling from the peak, the H₂O-isopleths are subparallel to the *P–T* path for the Micaschist zone and the Upper Moravian nappe, consistent with little mineralogical change in sample Vr7b, and with sillimanite–biotite replacing garnet in sample Vr1a via the H₂O-conserving consumption of muscovite. On further cooling, pseudosection modelling predicts mineralogical changes that require addition of H₂O. Growth of chlorite in all the samples is therefore consistent with addition of H₂O within the chlorite stability field, below 560–580°C, and therefore with external fluid circulation below these conditions.

Monazite history as recorded by its composition and texture

Significance of monazite type and texture

Monazite is rare and below 5 µm in size in the staurolite–chlorite zone (sample L82); rare, small (occasionally

reaching >50 µm) and irregular in shape in the staurolite zone (sample L159); and large (>50 µm in size) and more abundant in the kyanite and kyanite–sillimanite zones (samples Vr7b and Vr1a). Irrespective of the monazite-forming reaction, this is interpreted as the onset and limited prograde monazite growth at staurolite grade at 5.5 kbar and 570°C, and continued abundant prograde monazite growth after the kyanite-in reaction at 7.5 kbar and 630°C (e.g. Gasser *et al.*, 2012; Wing *et al.*, 2003; Fig. 12).

Monazite was found included in garnet, staurolite and kyanite, indicating monazite crystallization prior to or simultaneous with crystallization of these porphyroblasts. Because there is a correlation of monazite size with metamorphic grade, we interpret monazite included in staurolite and kyanite as a result of their simultaneous crystallization beyond the staurolite-in and kyanite-in reactions (Fig. 12). Because of the correlation of monazite size with metamorphic grade, monazite in the matrix is also interpreted as forming on the prograde *P–T* path.

Significance of trace element patterns in monazite

Monazite is zoned, and the various zones in the compositional maps have rather sharp boundaries and irregular embayments, especially in Y, that are usually interpreted as a result of monazite recrystallization in the presence of fluids (Figs 7 and 8) (Kelly *et al.*, 2012, and references therein). However, there is a different kind of zoning for grains included in porphyroblasts and matrix grains. In the kyanite zone, the grains in kyanite and biotite have high-Y cores, whereas grain 191-1 from the matrix is patchy with most of the grain showing a low Y content and only limited islands of high Y (Fig. 7). Detailed examination of this grain shows internal ‘boundaries’ with shapes indicative of dynamic recrystallization (Fig. 9). Independent of the origin of these internal boundaries, the boundaries may have facilitated fluid migration and therefore more extensive recrystallization of this grain (reflected also in its significantly lower age; Fig. 10b). In the kyanite–sillimanite zone (Vr1a) the monazite included in garnet and staurolite is different

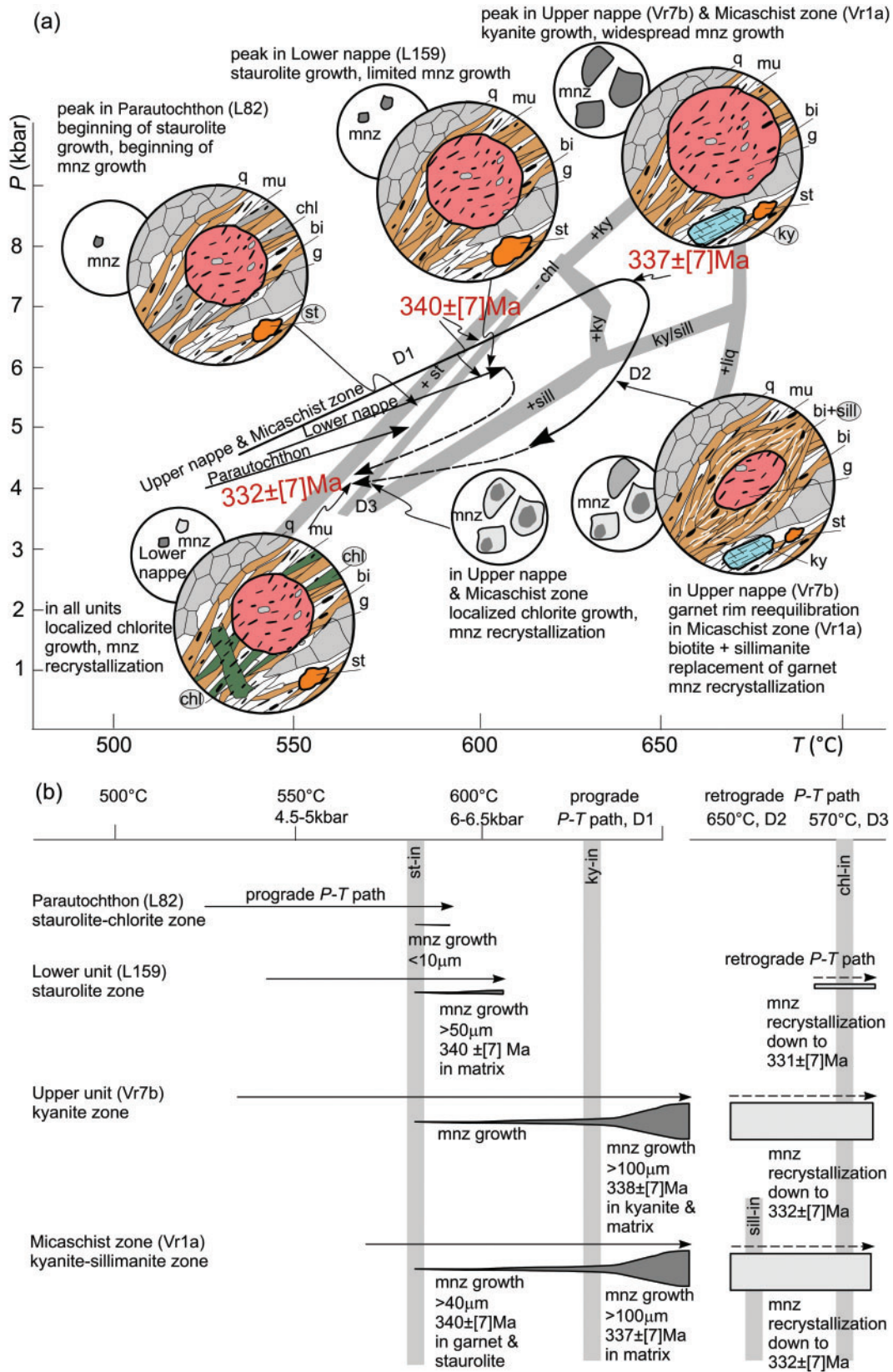


Fig. 12. (a) Summary of inferred P - T - d paths with interpretative sketches of major mineral and monazite crystallization and recrystallization, combined with monazite ages. (b) Interpretation of monazite crystallization, abundance and ages along prograde and retrograde parts of the P - T path. The two groups of data, $340\text{--}337 \pm [7]$ Ma and $332 \pm [7]$ Ma, in the context of the in-run uncertainties are distinct and indicate a 9 ± 3 Myr period of monazite (re)crystallization.

from that in the matrix. Monazite in garnet and staurolite has high Y with only a limited Y drop at the rim. The grains in the matrix show high Y in the core with a wide low-Y zone and narrow Y-rich rims, or low-Y cores with narrow Y-rich rims (Fig. 8). The different type of zoning in the monazite inclusions and matrix is interpreted in accordance with Kelly *et al.* (2012) as a result of more extensive fluid-assisted recrystallization in the matrix. Porphyroblasts shield monazite inclusions from recrystallization to a certain extent, but irregular embayments in some of the inclusions show that some fluid may have entered along cleavage planes or cracks after occlusion. Matrix monazite shows thicker embayments in Y, and in some cases two distinct chemical zones, suggesting more advanced recrystallization after formation (Kelly *et al.*, 2012).

Monazite analyses are compared in Fig. 11 with the staurolite–kyanite–sillimanite schist sample 22 of Mottram *et al.* (2014), who described a trend of increasing HREE from core to rim of monazite and correlated REE patterns in monazite and garnet profiles. Monazite shows increasing spread in the HREE concentrations from the staurolite zone (L159) to the kyanite–sillimanite zone (Vr1a). The monazite HREE concentrations in the staurolite zone are low, and have trends similar to the monazite cores from sample 22 of Mottram *et al.* (2014). In the kyanite zone (Vr7b), patchy matrix monazite grain 191-1 shows slightly higher HREE compared with the staurolite zone monazite (L159), and monazite in kyanite and biotite has even higher HREE, comparable with the monazite rims of Mottram *et al.* (2014). In the staurolite zone, monazite in garnet and staurolite and some matrix monazite grains have HREE comparable with the monazite cores of sample 22 of Mottram *et al.* (2014), whereas some matrix grains show higher HREE concentrations, comparable with the rims of monazite in sample 22 (Mottram *et al.*, 2014). Mottram *et al.* (2014) reported a systematic increase in Y content with decreasing monazite age. A similar trend exists in the Thaya window monazite: the HREE concentrations increase from 344 to 335 Ma, followed by a drop to lower levels until 328 Ma (Fig. 11d and e).

The sharp drop in HREE and Yb/Gd at 335–328 Ma (Fig. 11d and e) may be qualitatively compared with monazite Y maps in Figs 7 and 8, which show numerous sharp embayments with low Y values into high-Y cores—a pattern classically interpreted as a result of fluid-assisted recrystallization (Kelly *et al.*, 2012). The ages do not always correlate with the maps, possibly as a result of unknown three-dimensional geometry. Many data points between 335 and 329 Ma are from the grain with low and patchy Y (Vr7b-191-1) that has subgrain boundaries (perhaps owing to dynamic recrystallization; Fig. 9) that may have facilitated fluid migration and led to more extensive recrystallization. Based on the geometry of the low-Y embayments and internal structure of grain Vr7b-191-1, we interpret the 335–328 Ma monazite analyses with low HREE and low Yb/Gd ratio as a result of fluid-assisted recrystallization. The Eu

anomaly in all the samples is variably positive or negative, and deep or shallow, independent of the monazite texture, and is interpreted as a result of monazite growth near or distant to plagioclase.

Monazite ages in the context of the *P–T–d* path

The single ^{207}Pb -corrected $^{238}\text{U}/^{206}\text{Pb}$ spot dates for monazite from the three studied samples, irrespective of metamorphic grade, range from 344 to 330 Ma (Fig. 10). Grouping of the data into isochrons leads to a narrower range from $340 \pm [7]$ Ma to $331 \pm [7]$ Ma; the in-run uncertainties on samples L159, Vr7b and Vr1a indicate a 9 ± 3 Myr period of monazite (re)crystallization. In the staurolite zone (L159), monazite from the matrix shows a range from 340 to $331 \pm [7]$ Ma. In the kyanite zone (Vr7b), monazite included in kyanite $337 \pm [7]$ Ma, included in biotite is $338 \pm [7]$ Ma, and in some patchy-zoned (dynamically recrystallized?) matrix monazite is $338 \pm [7]$ Ma, whereas the youngest spots from the same grain are $332 \pm [7]$ Ma. In the kyanite–sillimanite zone, monazite included in garnet gives $340 \pm [7]$ Ma, in staurolite $337 \pm [7]$ Ma, and the matrix monazite shows a spread of dates from 340 to $330 \pm [7]$ Ma. The ages from monazite inclusions are interpreted as approximately dating the staurolite and kyanite-in reactions along the prograde path at $340\text{--}337 \pm [7]$ Ma, respectively (Fig. 12). The ages from the matrix monazite (and some inclusions) are interpreted as dating both the prograde crystallization of monazite at $340\text{--}337 \pm [7]$ Ma, and its (re)crystallization at or down to $332 \pm [7]$ Ma. The presence of chlorite implies the limited external availability of fluid on the retrograde *P–T* path. Migration of this fluid is likely to have been responsible for heterogeneous fluid-assisted recrystallization and isotopic resetting of the originally prograde monazite, even where included in garnet, staurolite and kyanite. It is suggested that the rocks passed below the chlorite-in reaction on the retrograde path at $332 \pm [7]$ Ma.

TECTONIC IMPLICATIONS

The new metamorphic and geochronological data provided by this study have profound implications for our understanding of tectonometamorphic processes during interaction between a hot orogenic root (the Moldanubian) and a rigid promontory (the Brunia microcontinent) during continental collision at the eastern margin of the Bohemian Massif (Figs 12 and 13). As the in-run uncertainties on ^{207}Pb -corrected $^{238}\text{U}/^{206}\text{Pb}$ monazite ages are 1–3 Ma, they indicate a 9 ± 3 Myr period of monazite (re)crystallization during tectonometamorphic processes within the Thaya window. The $340\text{--}337 \pm [7]$ Ma, Early Carboniferous, age of prograde metamorphism may be interpreted as the time when the Brunia promontory was thrust underneath the hot Moldanubian root (deformation D_1 , Fig. 13a). This age corresponds to the time of the peak metamorphic event reported from most of the granulite

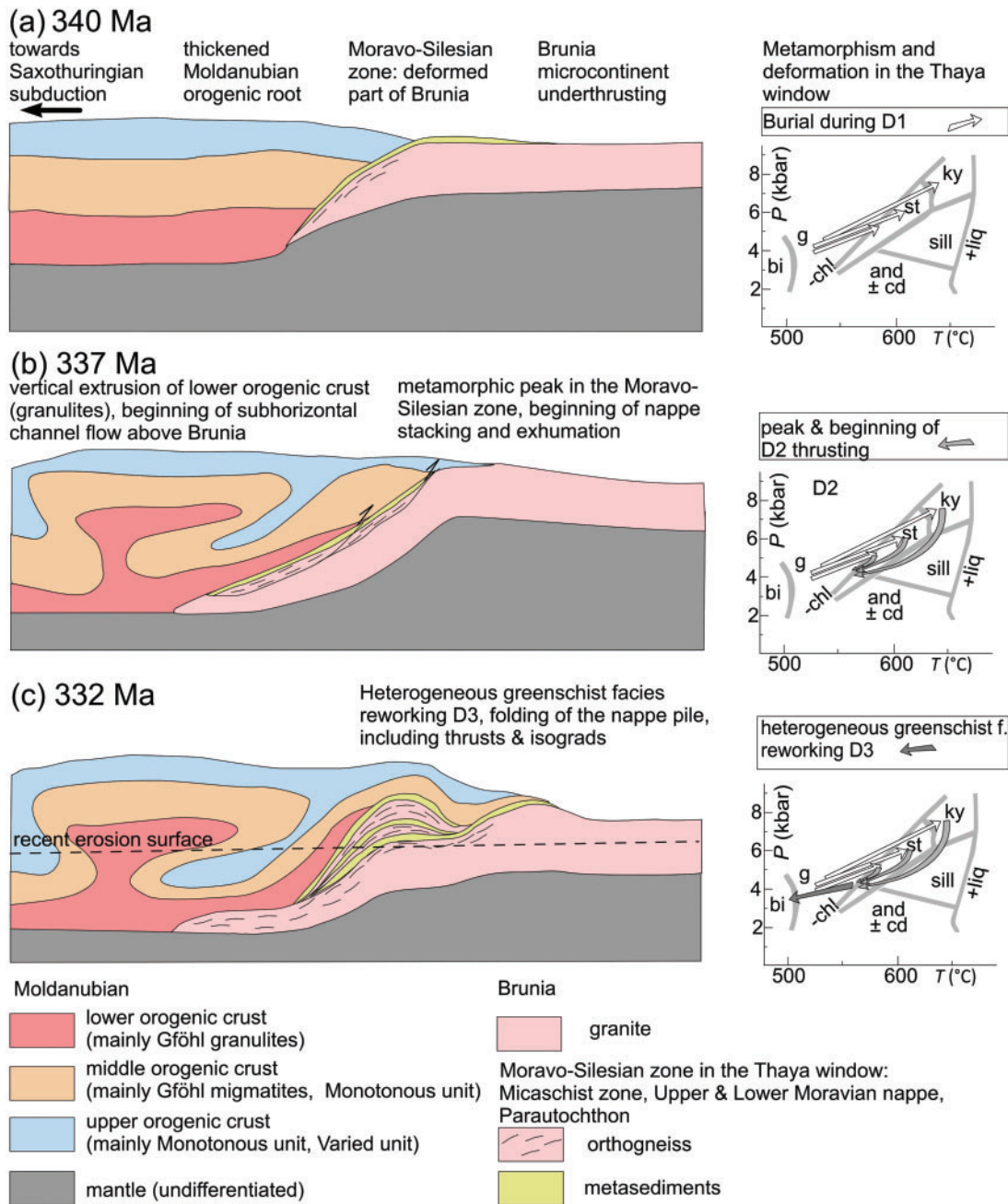


Fig. 13. Tectonic sketches correlating deformation events, P - T paths and monazite data in the Thaya window of the Moravo-Silesian zone with the evolution of the Moldanubian domain. The schematic P - T diagrams are based on calculated pseudosections; stability of index minerals is indicated in the sense of the clockwise P - T path. (For discussion see text.)

massifs of the Moldanubian domain (e.g. Van Breemen *et al.*, 1982; Kröner *et al.*, 2000; Janoušek *et al.*, 2004; Schulmann *et al.*, 2005; Sláma *et al.*, 2008; Friedl *et al.*, 2011). Recent studies suggest that the emblematic 340 Ma U-Pb zircon age from the granulite massifs reflects the beginning of exhumation, not burial (Roberts & Finger, 1997; Franěk *et al.*, 2011; Friedl *et al.*, 2011; Skrzypek *et al.*, 2012). Therefore, it can be speculated that the indentation of Brunia induced the vertical upwelling of the orogenic lower crust in the antiformal belt parallel to the Brunia margin (Schulmann *et al.*, 2009; Lexa *et al.*, 2011). Subsequent horizontal channel

flow of the hot Moldanubian material over the advancing Brunia indenter (Ráček *et al.*, 2006; Hasalová *et al.*, 2008; Schulmann *et al.*, 2008; Štípská *et al.*, 2008; Maierová *et al.*, 2014) may be related to the imbrication of the western margin of the Brunia, involving progressive migration of the thrust downwards, attachment of the Moravian nappes to the hanging-wall Moldanubian root, and therefore migration of the intraplate boundary downwards (deformation D₂, Fig. 13b) (Štípská & Schulmann, 1995; Štípská *et al.*, 2000). The thrusting of the Brunia-derived nappes occurs at decreasing P - T conditions, disrupts the metamorphic isograds attained

at peak and causes their inversion, including inversion within a single nappe sheet (Štípská & Schulmann, 1995).

The monazite ages of $332 \pm [7]$ Ma probably reflect reactivation of the nappe pile (deformation D₃, Fig. 13c) and the formation of greenschist-facies shear zones in both the Moravian nappes (Schulmann *et al.*, 1994; Kolaříková *et al.*, 1997) and the overlying Moldanubian migmatites during renewed dextral transpressive movement of the Brunia microcontinent, which also caused late crustal-scale folding of the Moravian nappe pile (Fig. 13c) (Fritz & Neubauer, 1993; Schulmann *et al.*, 1994). The late D₃ event folded not only the nappes, but also the thrusts and mineral isograds, causing their apparent oblique relationships in the recent erosion surface (Fig. 2) (Štípská & Schulmann, 2000). The muscovite ⁴⁰Ar/³⁹Ar ages (326–329 Ma) reported from the Moravian zone and the adjacent Moldanubian domain (Dallmeyer *et al.*, 1992; Fritz *et al.*, 1996) reflect post-folding cooling of the whole nappe stack.

ACKNOWLEDGEMENTS

R. Čopjaková and R. Škoda of the Institute of Geosciences, Masaryk University, Brno are thanked for operating the microprobe. Pavel Pitra and two other reviewers are thanked for their constructive reviews, and Alasdair Skelton is thanked for his editorial work.

FUNDING

We gratefully acknowledge the financial support of the Czech National Grant Agency (13-16315S to P.S. and Ondrej Lexa), the French National Grant Agency (ANR-DSP-Tibet to K.S.) and the National Science Foundation (EAR-1219942 to B.R.H.).

SUPPLEMENTARY DATA

Supplementary data for this paper are available at *Journal of Petrology* online.

REFERENCES

- Aleinikoff, J. N. (2006). Deciphering igneous and metamorphic events in high grade rocks of the Wilmington Complex, Delaware: Morphology, CL and BSE zoning, and SHRIMP U–Pb geochronology of zircon and monazite. *Geological Society of America Bulletin* **118**, 39–64.
- Andreasson, P. G. & Lagerblad, B. (1980). Occurrence and significance of inverted metamorphic gradients in the western Scandinavian Caledonides. *Journal of the Geological Society, London* **137**, 219–230.
- Arenas, R., Rubio Pascual, F. J., Díaz García, F. & Martínez Catálan, J. R. (1995). High-pressure micro-inclusions and development of an inverted metamorphic gradient in the Santiago Schists (Ordenes Complex, NW Iberian Massif, Spain): evidence of subduction and syncollisional decompression. *Journal of Metamorphic Geology* **13**, 141–164.
- Ayers, J. C., Miller, C., Gorisch, B. & Milleman, J. (1999). Textural development of monazite during high-grade metamorphism: Hydrothermal growth kinetics, with implications for U,Th–Pb geochronology. *American Mineralogist* **84**, 1766–1780.
- Barcheck, C. G., Wiens, W. A., Van Keken, P. E. & Hacker, B. R. (2012). The relationship of intermediate- and deep-focus seismicity to the hydration and dehydration of subducting slabs. *Earth and Planetary Science Letters* **349–350**, 153–160.
- Bordet, P. (1961). *Recherches géologiques dans l'Himalaya du Népal, région du Makalu*. Centre National de la Recherche Scientifique, 275 pp.
- Bröcker, M., Klemd, R., Kooijman, E., Berndt, J. & Larionov, A. (2010). Zircon geochronology and trace element characteristics of eclogites and granulites from the Orlica–Sněžník complex, Bohemian Massif. *Geological Magazine* **147**, 339–362.
- Burg, J.-P., Leyreloup, A. F., Marchand, J. & Matte, P. (1984). Inverted metamorphic zonation and large-scale thrusting in the Variscan Belt: an example in the French Massif Central. In: Hutton, D. H. W. & Sanderson, D. J. (eds) *Variscan Tectonics of the North Atlantic Region*. Geological Society, London, *Special Publications* **14**, 47–61.
- Caddick, M. J., Bickle, M. J., Harris, N. B. W., Holland, T. J. B., Horstwood, M. S. A., Parrish, R. R. & Ahmad, T. (2007). Burial and exhumation history of a Lesser Himalayan schist: Recording the formation of an inverted metamorphic sequence in NW India. *Earth and Planetary Science Letters* **264**, 375–390.
- Camiré, G. (1995). Development of inverted metamorphic gradient in the internal domain of the Taconian belt, Gaspé Peninsula. *Canadian Journal of Earth Sciences* **32**, 37–51.
- Carosi, R., Montomoli, C., Rubatto, D. & Visonà, D. (2010). Late Oligocene high-temperature shear zones in the core of the Higher Himalayan Crystallines (Lower Dolpo, western Nepal). *Tectonics* **29**, TC4029.
- Catlos, E. J., Gilley, L. D. & Harrison, T. M. (2002). Interpretation of monazite ages obtained via *in situ* analysis. *Chemical Geology* **188**, 193–215.
- Catlos, E. J., Dubey, C. S., Harrison, T. M. & Edwards, M. A. (2004). Late Miocene movement within the Himalayan Main Central Thrust shear zone, Sikkim, north-east India. *Journal of Metamorphic Geology* **22**, 207–226.
- Cherniak, D. J., Watson, E. B., Grove, M. & Harrison, T. M. (2004). Pb diffusion in monazite: A combined RBS/SIMS study. *Geochimica et Cosmochimica Acta* **68**, 829–840.
- Coggon, R. & Holland, T. J. B. (2002). Mixing properties of phengitic micas and revised garnet–phengite thermobarometers. *Journal of Metamorphic Geology* **20**, 683–696.
- Compston, W., Williams, I. S., Kirschvink, J. L., Zhang, Z. & Ma, G. (1992). Zircon U–Pb ages for the Early Cambrian time-scale. *Journal of the Geological Society, London* **149**, 171–184.
- Connolly, J. A. D. (2005). Computation of phase equilibria by linear programming: A tool for geodynamic modeling and its application to subduction zone decarbonation. *Earth and Planetary Science Letters* **236**, 524–541.
- Crowley, J. L. & Ghent, E. D. (1999). An electron microprobe study of the U–Th–Pb systematics of metamorphosed monazite: The role of Pb diffusion versus overgrowth and recrystallization. *Chemical Geology* **157**, 285–302.
- Dahl, P. S., Terry, M. P., Jercinovic, M. J., Williams, M. L., Hamilton, M. A., Foland, K. A., Clement, S. M. & Friberg, L. V. M. (2005). Electron probe (Ultrachron) microchronometry of metamorphic monazite: Unraveling the timing of polyphase thermotectonism in the easternmost Wyoming Craton (Black Hills, South Dakota). *American Mineralogist* **90**, 1712–1728.

- Dallmeyer, R. D., Neubauer, F. & Höck, V. (1992). Chronology of late Paleozoic tectonothermal activity in the southeastern Bohemian Massif, Austria (Moldanubian and Moravo-Silesian zones): $^{40}\text{Ar}/^{39}\text{Ar}$ mineral age controls. *Tectonophysics* **210**, 135–153.
- Didier, A., Bosse, V., Boulvais, P., Boulton, J., Paquette, J. L., Montel, J. M. & Devidal, J. L. (2013). Disturbance versus preservation of U–Th–Pb ages in monazite during fluid–rock interaction: Textural, chemical and isotopic *in situ* study in microgranites (Velay Dome, France). *Contributions to Mineralogy and Petrology* **165**, 1051–1072.
- Dudek, A. (1980). The crystalline basement block of the Outer Carpathians in Moravia–Brunovistulicum. *Rozprawy Československé Akademie Věd* **90**, 1–85.
- Dumond, G., McLean, N., Williams, M. L., Jercinovic, M. J. & Bowring, S. A. (2008). High-resolution dating of granite petrogenesis and deformation in a lower crustal shear zone: Athabasca granulite terrane, western Canadian Shield. *Chemical Geology* **254**, 175–196.
- Edel, J. B., Schulmann, K. & Holub, F. V. (2003). Anticlockwise and clockwise rotations of the Eastern Variscides accommodated by dextral lithospheric wrenching: palaeomagnetic and structural evidence. *Journal of the Geological Society, London* **160**, 209–218.
- Foster, G., Kinny, P., Vance, D., Prince, C. & Harris, N. (2000). The significance of monazite U–Th–Pb age data in metamorphic assemblages; a combined study of monazite and garnet chronometry. *Earth and Planetary Science Letters* **181**, 327–340.
- Franěk, J., Schulmann, K., Lexa, O., Ulrich, S., Štípská, P., Haloda, J. & Týcová, P. (2011). Origin of felsic granulite microstructure by heterogeneous decomposition of alkali feldspar and extreme weakening of orogenic lower crust during the Variscan orogeny. *Journal of Metamorphic Geology* **29**, 103–130.
- Friedl, G., Finger, F., Paquette, J., Quadt, A., McNaughton, N. & Fletcher, I. (2004). Pre-Variscan geological events in the Austrian part of the Bohemian Massif deduced from U–Pb zircon ages. *International Journal of Earth Sciences* **93**, 802–823.
- Friedl, G., Cooke, R. A., Finger, F., McNaughton, N. J. & Fletcher, I. R. (2011). Timing of Variscan HP–HT metamorphism in the Moldanubian Zone of the Bohemian Massif: U–Pb SHRIMP dating on multiply zoned zircons from a granulite from the Dunkelsteiner Wald Massif, Lower Austria. *Mineralogy and Petrology* **102**, 63–75.
- Fritz, H. & Loitzenbauer, J. (1994). Fluid activity during late stage of Variscan deformation in the Moravian nappe complex. *Mitteilungen der Österreichischen Mineralogischen Gesellschaft* **139**, 47–49.
- Fritz, H. & Neubauer, F. (1993). Kinematics of crustal stacking and dispersion in the south-eastern Bohemian Massif. *Geologische Rundschau* **82**, 556–565.
- Fritz, H., Dallmeyer, R. D. & Neubauer, F. (1996). Thick-skinned versus thin-skinned thrusting: Rheology controlled thrust propagation in the Variscan collisional belt (the Southeastern Bohemian Massif, Czech Republic–Austria). *Tectonics* **15**, 1389–1413.
- Fuchs, G. (1976). Zur Entwicklung der Böhmisches Masse. *Jahrbuch des Geologischen Bundesanstalts* **119**, 45–61.
- Gansser, A. (1964). *Geology of the Himalayas*. Interscience, 289 pp.
- Gasser, D., Bruand, E., Rubatto, D. & Stüwe, K. (2012). The behaviour of monazite from greenschist facies phyllites to anatectic gneisses: An example from the Chugach Metamorphic Complex, southern Alaska. *Lithos* **134–135**, 108–122.
- Gibson, H. D., Brown, R. L. & Parrish, R. R. (1999). Deformation induced inverted metamorphic field gradients: an example from the southeastern Canadian Cordillera. *Journal of Structural Geology* **21**, 751–767.
- Graham, C. M. & England, P. C. (1976). Thermal regimes and regional metamorphism in vicinity of overthrust faults—an example of shear heating and inverted metamorphic zonation from Southern California. *Earth and Planetary Science Letters* **31**, 142–152.
- Harlov, D. E. & Hetherington, C. J. (2010). Partial high-grade alteration of monazite using alkali-bearing fluids: Experiment and nature. *American Mineralogist* **95**, 1105–1108.
- Harlov, D. E., Wirth, R. & Hetherington, C. J. (2011). Fluid-mediated partial alteration in monazite: The role of coupled dissolution–reprecipitation in element redistribution and mass transfer. *Contributions to Mineralogy and Petrology* **162**, 329–348.
- Harrison, T. M., Ryerson, F. J., Le Fort, P., Yin, A., Lovera, O. M. & Catlos, E. J. (1997). A Late Miocene–Pliocene origin for the Central Himalayan inverted metamorphism. *Earth and Planetary Science Letters* **146**, E1–E7.
- Hasalová, P., Štípská, P., Powell, R., Schulmann, K., Janoušek, V. & Lexa, O. (2008). Transforming mylonitic metagranite by open-system interactions during melt flow. *Journal of Metamorphic Geology* **26**, 55–80.
- Hermann, J. & Rubatto, D. (2003). Relating zircon and monazite domains to garnet growth zones: Age and duration of granulite facies metamorphism in the Val Malenco lower crust. *Journal of Metamorphic Geology* **21**, 833–852.
- Hetherington, C. J., Harlov, D. E. & Budzyń, B. (2010). Experimental metasomatism of monazite and xenotime: Mineral stability, REE mobility and fluid composition. *Mineralogy and Petrology* **99**, 165–184.
- Höck, V. (1975). Mineralzonen in Metapeliten und Metapsammiten der Moravischen Zone in Niederoesterreich. *Mitteilungen der Geologischen Gesellschaft* **66–67**, 49–60.
- Höck, V., Marschallinger, R. & Topa, D. (1990). Granat–biotit–geothermometrie in metapeliten der Moravischen Zone in Österreich. *Österreichische Beiträge zu Meteorologie und Geophysik* **3**, 149–167.
- Hoisch, T. D., Wells, M. L. & Grove, M. (2008). Age trends in garnet-hosted monazite inclusions from upper amphibolite facies schist in the northern Grouse Creek Mountains, Utah. *Geochimica et Cosmochimica Acta* **72**, 5505–5520.
- Holland, T. J. B. & Powell, R. (1998). An internally consistent thermodynamic data set for phases of petrological interest. *Journal of Metamorphic Geology* **16**, 309–343.
- Holland, T. J. B. & Powell, R. (2003). Activity–composition relations for phases in petrological calculations: an asymmetric multicomponent formulation. *Contributions to Mineralogy and Petrology* **145**, 492–501.
- Holland, T. J. B., Baker, J. M. & Powell, R. (1998). Mixing properties and activity–composition relationships of chlorites in the system $\text{MgO–FeO–Al}_2\text{O}_3\text{–SiO}_2\text{–H}_2\text{O}$. *European Journal of Mineralogy* **10**, 395–406.
- Janots, E. & Wirth, R. (2012). Low-temperature alteration of monazite: Fluid mediated coupled dissolution–precipitation, irradiation damage, and disturbance of the U–Pb and Th–Pb chronometers. *Chemical Geology* **330–331**, 140–158.
- Janots, E., Engi, M., Berger, A., Allaz, J., Schwarz, J. O. & Spandler, C. (2008). Prograde metamorphic sequence of REE minerals in pelitic rocks of the Central Alps: Implications for allanite–monazite–xenotime phase relations from 250 to 610°C. *Journal of Metamorphic Geology* **26**, 509–526.

- Janots, E., Engi, M., Rubatto, D., Berger, A., Gregory, C. & Rahn, M. (2009). Metamorphic rates in collisional orogeny from *in situ* allanite and monazite dating. *Geology* **37**, 11–14.
- Janoušek, V. & Holub, F. V. (2007). The causal link between HP–HT metamorphism and ultrapotassic magmatism in collisional orogens: case study from the Moldanubian Zone of the Bohemian Massif. *Proceedings of the Geologists' Association* **118**, 75–86.
- Janoušek, V., Finger, F., Roberts, M., Frýda, J., Pin, C. & Dolejš, D. (2004). Deciphering the petrogenesis of deeply buried granites: whole-rock geochemical constraints on the origin of largely undepleted felsic granulites from the Moldanubian Zone of the Bohemian Massif. *Transactions of the Royal Society of Edinburgh: Earth Sciences* **95**, 141–159.
- Kellett, D. A., Grujic, D., Warren, C., Cottle, J., Jamieson, R. & Tenzin, T. (2010). Metamorphic history of a syn-convergent orogen-parallel detachment: The South Tibetan detachment system, Bhutan Himalaya. *Journal of Metamorphic Geology* **28**, 785–808.
- Kelly, N. M., Harley, S. L. & Möller, A. (2012). Complexity in the behavior and recrystallization of monazite during high-*T* metamorphism and fluid infiltration. *Chemical Geology* **322–323**, 192–208.
- Kelsey, D. E., Clark, C. & Hand, M. (2008). Thermobarometric modelling of zircon and monazite growth in melt-bearing systems: Examples using model metapelitic and metapsammitic granulites. *Journal of Metamorphic Geology* **26**, 199–212.
- Kingsbury, J. A., Miller, C. F., Wooden, J. L. & Harrison, T. M. (1993). Monazite paragenesis and U–Pb systematics in rocks of the eastern Mojave Desert, California, U.S.A.: implications for thermochronometry. *Chemical Geology* **110**, 147–167.
- Kohn, M. J., Wieland, M. S., Parkinson, C. D. & Upreti, B. N. (2005). Five generations of monazite in Langtang gneisses: Implications for chronology of the Himalayan metamorphic core. *Journal of Metamorphic Geology* **23**, 399–406.
- Kolaříková, A., Marquer, D. & Schulmann, K. (1997). Evolution of mass-transfer during progressive oblique under-thrusting of the Variscan foreland: eastern Bohemian Massif. *Geodinamica Acta* **10**, 81–93.
- Konopásek, J., Schulmann, K. & Johan, V. (2002). Eclogite-facies metamorphism at the eastern margin of the Bohemian Massif—Subduction prior to continental underthrusting? *European Journal of Mineralogy* **14**, 701–713.
- Kröner, A., O'Brien, P. J., Nemchin, A. A. & Pidgeon, R. T. (2000). Zircon ages for high pressure granulites from South Bohemia, Czech Republic, and their connection to Carboniferous high temperature processes. *Contributions to Mineralogy and Petrology* **138**, 127–142.
- Kylander-Clark, A. R. C., Hacker, B. R. & Cottle, J. M. (2013). Laser-ablation split-stream ICP petrochronology. *Chemical Geology* **345**, 99–112.
- Lanzirotti, A. & Hanson, G. N. (1996). Geochronology and geochemistry of multiple generations of monazite from the Wepawaug Schist, Connecticut, USA: Implications for monazite stability in metamorphic rocks. *Contributions to Mineralogy and Petrology* **125**, 332–340.
- Lexa, O., Schulmann, K., Janoušek, V., Štípská, P., Guy, A. & Racek, M. (2011). Heat sources and trigger mechanisms of exhumation of HP granulites in Variscan orogenic root. *Journal of Metamorphic Geology* **29**, 79–102.
- Ludwig, K. R. (2003). *Isoplot 3.00. A Geochronological Toolkit for Microsoft Excel*. Berkeley Geochronology Center Special Publication **4**.
- Mahar, E. M., Baker, J. M., Powell, R., Holland, T. J. B. & Howell, N. (1997). The effect of Mn on mineral stability in metapelites. *Journal of Metamorphic Geology* **15**, 223–238.
- Maierová, P., Lexa, O., Schulmann, K. & Štípská, P. (2014). Contrasting tectono-metamorphic evolution of orogenic lower crust in the Bohemian Massif: A numerical model. *Gondwana Research* **25**, 509–521.
- Martin, A. J., Gehrels, G. E. & DeCelles, P. G. (2007). The tectonic significance of (U,Th)/Pb ages of monazite inclusions in garnet from the Himalaya of central Nepal. *Chemical Geology* **244**, 1–24.
- Mottram, C. M., Warren, C. J., Regis, D., Roberts, N. M. W., Harris, N. B. W., Argles, T. W. & Parrish, R. R. (2014). Developing an inverted Barrovian sequence; insights from monazite petrochronology. *Earth and Planetary Science Letters* **403**, 418–431.
- Nahodilová, R., Štípská, P., Powell, R., Košler, J. & Racek, M. (2014). High-Ti muscovite as a prograde relict in high pressure granulites with metamorphic Devonian zircon ages (Běstvína granulite body, Bohemian Massif): Consequences for the relamination model of subducted crust. *Gondwana Research* **25**, 630–648.
- Palin, R. M., Searle, M. P., St-Onge, M. R., Waters, D. J., Roberts, N. M. W., Horstwood, M. S. A., Parrish, R. R. & Weller, O. M. (2014). Two-stage cooling history of pelitic and semi-pelitic mylonite (*sensu lato*) from the Dongjiu–Milin shear zone, northwest flank of the eastern Himalayan syntaxis. *Gondwana Research* <http://dx.doi.org/10.1016/j.gr.2014.07.009>.
- Paton, C., Hellstrom, J. C., Paul, B., Woodhead, J. D. & Hergt, J. M. (2011). Lolite: freeware for the visualisation and processing of mass spectrometer data. *Journal of Analytical Atomic Spectrometry* **26**, 2508–2518.
- Pitra, P., Ballèvre, M. & Ruffet, G. (2010). Inverted metamorphic field gradient towards a Variscan suture zone (Champtoceaux Complex, Armorican Massif, France). *Journal of Metamorphic Geology* **28**, 183–208.
- Poitrasson, F., Chenery, S. & Shepherd, T. J. (2000). Electron microprobe and LA-ICP-MS study of monazite hydrothermal alteration: Implications for U–Th–Pb geochronology and nuclear ceramics. *Geochimica et Cosmochimica Acta* **64**, 3283–3297.
- Prince, C. I., Košler, J., Vance, D. & Gunther, D. (2000). Comparison of laser ablation ICP-MS and isotope dilution REE analyses—implications for Sm–Nd garnet geochronology. *Chemical Geology* **168**, 255–274.
- Putnis, A. (2002). Mineral replacement reactions: From macroscopic observations to microscopic mechanisms. *Mineralogical Magazine* **66**, 689–708.
- Pyle, J. M. & Spear, F. S. (2003). Four generations of accessory-phase growth in low-pressure migmatites from SW New Hampshire. *American Mineralogist* **88**, 338–351.
- Pyle, J. M., Spear, F. S., Rudnick, R. L. & McDonough, W. F. (2001). Monazite–xenotime–garnet equilibrium in metapelites and a new monazite–garnet thermometer. *Journal of Petrology* **42**, 2083–2107.
- Racek, M., Štípská, P., Pitra, P., Schulmann, K. & Lexa, O. (2006). Metamorphic record of burial and exhumation of orogenic lower and middle crust: a new tectonothermal model for the Drosendorf window (Bohemian Massif, Austria). *Mineralogy and Petrology* **86**, 221–251.
- Rasmussen, B., Muhling, J. R., Fletcher, I. R. & Wingate, M. T. D. (2006). *In situ* SHRIMP U–Pb dating of monazite integrated with petrology and textures: Does bulk composition control whether monazite forms in low-Ca pelitic rocks during amphibolite facies metamorphism? *Geochimica et Cosmochimica Acta* **70**, 3040–3058.

- Roberts, M. P. & Finger, F. (1997). Do U–Pb zircon ages from granulites reflect peak metamorphic conditions? *Geology* **25**, 319–322.
- Rubatto, D., Williams, I. S. & Buick, I. S. (2001). Zircon and monazite response to prograde metamorphism in the Reynolds Range, central Australia. *Contributions to Mineralogy and Petrology* **140**, 458–468.
- Rubatto, D., Hermann, J. & Buick, I. S. (2006). Temperature and bulk composition control on the growth of monazite and zircon during low-pressure anatexis (Mount Stafford, Central Australia). *Journal of Petrology* **47**, 1973–1996.
- Rubatto, D., Chakraborty, S. & Dasgupta, S. (2013). Timescales of crustal melting in the Higher Himalayan Crystallines (Sikkim, Eastern Himalaya) inferred from trace element-constrained monazite and zircon chronology. *Contributions to Mineralogy and Petrology* **165**, 349–372.
- Schulmann, K. (1990). Fabric and kinematic study of the Bíteš orthogneiss (Southwestern Moravia)—Result of large-scale northeastward shearing parallel to the Moldanubian–Moravian boundary. *Tectonophysics* **177**, 229–244.
- Schulmann, K., Ledru, P., Autran, A., Melka, R., Lardeaux, J. M., Urban, M. & Lobkowicz, M. (1991). Evolution of nappes in the eastern margin of the Bohemian Massif—a kinematic interpretation. *Geologische Rundschau* **80**, 73–92.
- Schulmann, K., Melka, R., Lobkowicz, M., Ledru, P., Lardeaux, J. M. & Autran, A. (1994). Contrasting styles of deformation during progressive nappe stacking at the southeastern margin of the Bohemian Massif (Thaya Dome). *Journal of Structural Geology* **16**, 355–370.
- Schulmann, K., Kröner, A., Hegner, E., Wendt, I., Konopásek, J., Lexa, O. & Štípská, P. (2005). Chronological constraints on the pre-orogenic history, burial and exhumation of deep-seated rocks along the eastern margin of the Variscan orogen, Bohemian Massif, Czech Republic. *American Journal of Science* **305**, 407–448.
- Schulmann, K., Lexa, O., Štípská, P., Racek, M., Tajčmanová, L., Konopásek, J., Edel, J. B., Peschler, A. & Lehmann, J. (2008). Vertical extrusion and horizontal channel flow of orogenic lower crust: key exhumation mechanisms in large hot orogens? *Journal of Metamorphic Geology* **26**, 273–297.
- Schulmann, K., Konopásek, J., Janoušek, V., Lexa, O., Lardeaux, J. M., Edel, J. B., Štípská, P. & Ulrich, S. (2009). An Andean type Palaeozoic convergence in the Bohemian Massif. *Comptes Rendus Géoscience* **341**, 266–286.
- Seydoux-Guillaume, A. M., Paquette, J. L., Wiedenbeck, M., Montel, J. M. & Heinrich, W. (2002). Experimental resetting of the U–Th–Pb systems in monazite. *Chemical Geology* **191**, 165–181.
- Seydoux-Guillaume, A. M., Montel, J. M., Bingen, B., Bosse, V., de Parseval, P., Paquette, J. L., Janots, E. & Wirth, R. (2012). Low-temperature alteration of monazite: Fluid mediated coupled dissolution–precipitation, irradiation damage, and disturbance of the U–Pb and Th–Pb chronometers. *Chemical Geology* **330–331**, 140–158.
- Skrzypek, E., Štípská, P. & Cocherie, A. (2012). The origin of zircon and the significance of U–Pb ages in high-grade metamorphic rocks: A case study from the Variscan orogenic root (Vosges Mountains, NE France). *Contributions to Mineralogy and Petrology* **164**, 935–957.
- Sláma, J., Košler, J., Condon, D. J., Crowley, J. L., Gerdes, A., Hanchar, J. M., Horstwood, M. S. A., Morris, G. A., Nasdala, L., Norberg, N., Schaltegger, U., Schoene, B., Tubrett, M. N. & Whitehouse, M. J. (2008). Plešovice zircon—A new natural reference material for U–Pb and Hf isotopic microanalysis. *Chemical Geology* **249**, 1–35.
- Spear, F. S. (2010). Monazite–allanite phase relations in metapelites. *Chemical Geology* **279**, 55–62.
- Spear, F. S. & Pyle, J. M. (2002). Apatite, monazite, and xenotime in metamorphic rocks. In: Kohn, M. J., Rakovan, J. & Hughes, J. M. (eds) *Phosphates: Geochemical, geobiological, and materials importance. Mineralogical Society of America Reviews in Mineralogy and Geochemistry* Vol. 48, Washington, pp. 293–336.
- Stacey, J. S. & Kramers, J. D. (1975). Approximation of terrestrial lead isotope evolution by a two-stage model. *Earth and Planetary Science Letters* **26**, 207–221.
- Štípská, P. & Schulmann, K. (1995). Inverted metamorphic zonation in a basement-derived nappe sequence, eastern margin of the Bohemian Massif. *Geological Journal* **30**, 385–413.
- Štípská, P., Schulmann, K. & Höck, V. (2000). Complex metamorphic zonation of the Thaya dome: result of buckling and gravitational collapse of an imbricated nappe sequence. In: Cosgrove, J. W. & Ameen, M. S. (eds) *Forced Folds and Fractures. Geological Society, London, Special Publications* **169**, 197–211.
- Štípská, P., Schulmann, K. & Kröner, A. (2004). Vertical extrusion and middle crustal spreading of omphacite granulite: a model of syn-convergent exhumation (Bohemian Massif, Czech Republic). *Journal of Metamorphic Geology* **22**, 179–198.
- Štípská, P., Schulmann, K. & Powell, R. (2008). Contrasting metamorphic histories of lenses of high-pressure rocks and host migmatites with a flat orogenic fabric (Bohemian Massif, Czech Republic): a result of tectonic mixing within horizontal crustal flow? *Journal of Metamorphic Geology* **26**, 623–646.
- St-Onge, M. R., Wodicka, N. & Ijwliw, O. (2007). Polymetamorphic evolution of the trans-Hudson orogen, Baffin Island, Canada: Integration of petrological, structural and geochronological data. *Journal of Petrology* **48**, 271–302.
- Suess, F. E. (1912). Die Moravischen Fenster und ihre Beziehung zum Grundgebirge des Hohen Gesenkes. *Akademie der Wissenschaften, Denkschrift Mathematisch-Naturwissenschaftliche Klasse* **88**, 541–631.
- Suess, F. E. (1926). *Intrusionstektonik und Wandertektonik im variszischen Grundgebirge*. Borntraeger.
- Tajčmanová, L., Soejono, I., Konopásek, J., Košler, J. & Klötzli, U. (2010). Structural position of high-pressure felsic to intermediate granulites from NE Moldanubian domain (Bohemian Massif). *Journal of the Geological Society, London* **167**, 329–345.
- Townsend, K. J., Miller, C. F., D'Andrea, J. L., Ayers, J. C., Harrison, T. M. & Coath, C. D. (2001). Low temperature replacement of monazite in the Ireteba granite, Southern Nevada: Geochronological implications. *Chemical Geology* **172**, 95–112.
- Ulrich, S., Schulmann, K. & Casey, M. (2002). Microstructural evolution and rheological behaviour of marbles deformed at different crustal levels. *Journal of Structural Geology* **24**, 979–995.
- Van Breemen, O., Aftalion, M., Bowes, D. R., Dudek, A., Misař, Z., Povondra, P. & Vrána, S. (1982). Geochronological studies of the Bohemian massif, Czechoslovakia, and their significance in the evolution of Central Europe. *Transactions of the Royal Society of Edinburgh: Earth Sciences* **73**, 89–108.
- Vance, D., Müller, W. & Villa, I. M. (2003). Geochronology: Linking the isotopic record with petrology and textures—an introduction. In: *Geological Society, London, Special Publications* **220**, 1–24.
- Wawrzenitz, N., Krohe, A., Rhede, D. & Romer, R. L. (2012). Dating rock deformation with monazite: The impact of dissolution precipitation creep. *Lithos* **134–135**, 52–74.
- Weller, O. M., St-Onge, M. R., Waters, D. J., Rayner, N., Searle, M. P., Chung, S. L., Palin, R. M., Lee, Y. H. & Xu, X. (2013).

- Quantifying barrovian metamorphism in the Danba structural culmination of eastern Tibet. *Journal of Metamorphic Geology* **31**, 909–935.
- White, R. W., Powell, R., Holland, T. J. B. & Worley, B. A. (2000). The effect of TiO_2 and Fe_2O_3 on metapelitic assemblages at greenschist and amphibolite facies conditions: mineral equilibria calculations in the system $\text{K}_2\text{O}\text{--}\text{FeO}\text{--}\text{MgO}\text{--}\text{Al}_2\text{O}_3\text{--}\text{SiO}_2\text{--}\text{H}_2\text{O}\text{--}\text{TiO}_2\text{--}\text{Fe}_2\text{O}_3$. *Journal of Metamorphic Geology* **18**, 497–511.
- White, R. W., Powell, R. & Holland, T. J. B. (2007). Progress relating to calculation of partial melting equilibria for metapelites. *Journal of Metamorphic Geology* **25**, 511–527.
- Williams, M. L. & Jercinovic, M. J. (2002). Microprobe monazite geochronology: Putting absolute time into microstructural analysis. *Journal of Structural Geology* **24**, 1013–1028.
- Williams, M. L., Jercinovic, M. J., Harlov, D. E., Budzyń, B. & Hetherington, C. J. (2011). Resetting monazite ages during fluid-related alteration. *Chemical Geology* **283**, 218–225.
- Wing, B. A., Ferry, J. M. & Harrison, T. M. (2003). Prograde destruction and formation of monazite and allanite during contact and regional metamorphism of pelites: Petrology and geochronology. *Contributions to Mineralogy and Petrology* **145**, 228–250.